

# A Tale of Three Galaxies: Deciphering the Infrared Emission of the Spectroscopically Anomalous Galaxies IRAS F10398+1455, IRAS F21013-0739 and SDSS J0808+3948

DRAFT: 2024.3.2.2254

Yanxia Xie<sup>1,2</sup>, Aigen Li<sup>2</sup>, Lei Hao<sup>1</sup>, and Robert Nikutta<sup>3</sup>

## ABSTRACT

The *Spitzer*/Infrared Spectrograph spectra of three spectroscopically anomalous galaxies (IRAS F10398+1455, IRAS F21013-0739 and SDSS J0808+3948) are modeled in terms of a mixture of warm and cold silicate dust, and warm and cold carbon dust. Their unique infrared (IR) emission spectra are characterized by a steep  $\sim 5\text{--}8\,\mu\text{m}$  emission continuum, strong emission bands from polycyclic aromatic hydrocarbon (PAH) molecules, and prominent silicate emission. The steep  $\sim 5\text{--}8\,\mu\text{m}$  emission continuum and strong PAH emission features suggest the dominance of starbursts, while the silicate emission is indicative of significant heating from active galactic nuclei (AGNs). With warm and cold silicate dust of various compositions (“astronomical silicate,” amorphous olivine, or amorphous pyroxene) combined with warm and cold carbon dust (amorphous carbon, or graphite), we are able to closely reproduce the observed IR emission of these galaxies. We find that the dust temperature is the primary cause in regulating the steep  $\sim 5\text{--}8\,\mu\text{m}$  continuum and silicate emission, insensitive to the exact silicate or carbon dust mineralogy and grain size  $a$  as long as  $a \lesssim 1\,\mu\text{m}$ . More specifically, the temperature of the  $\sim 5\text{--}8\,\mu\text{m}$  continuum emitter (which is essentially carbon dust) of these galaxies is  $\sim 250\text{--}400\,\text{K}$ , much lower than that of typical quasars which is  $\sim 640\,\text{K}$ . Moreover, it appears that larger dust grains are preferred in quasars. The lower dust temperature and smaller grain sizes inferred for these three galaxies compared with that of quasars could be due to the fact that they may harbor a young/weak AGN which is not maturely developed yet.

---

<sup>1</sup>Shanghai Astronomical Observatory, Chinese Academy of Sciences, 80 Nandan Road, Shanghai 200030, China

<sup>2</sup>Department of Physics and Astronomy, University of Missouri, Columbia, MO 65211, USA

<sup>3</sup>Instituto de Astrofísica, Facultad de Física, Pontificia Universidad Católica de Chile, 306, Santiago 22, Chile

*Subject headings:* dust, extinction — galaxies: active — galaxies: individual (IRAS F10398+1455, IRAS F21013-0739, SDSS J0808+3948) — infrared: galaxies

## 1. Introduction

Dust is a ubiquitous feature of the cosmos. It is present in a wide variety of astrophysical systems, including active galactic nuclei (AGNs) and starburst galaxies. Amorphous silicates and some form of carbonaceous materials (e.g., graphite, amorphous carbon, and hydrogenated amorphous carbon) are thought to be the two dominant cosmic dust species. Silicate dust reveals its presence in AGN and starbursts through the 9.7 and 18  $\mu\text{m}$  spectral features which respectively arise from the Si–O stretching and O–Si–O bending vibrational modes (Henning 2010). The detection of the 3.4  $\mu\text{m}$  C–H stretching absorption feature in AGN indicates the presence of aliphatic, chain-like hydrocarbon dust in AGN (e.g., see Imanishi et al. 1997, Mason et al. 2004). Starbursts lack the 3.4  $\mu\text{m}$  absorption feature. This may be related to the fact that starbursts, particularly in their nuclear regions, are often heavily obscured by dust and ice. In the Milky Way, the 3.4  $\mu\text{m}$  absorption feature is seen in the diffuse interstellar medium (ISM), but not in dense clouds where the 3.1  $\mu\text{m}$  H<sub>2</sub>O ice absorption feature is strong (see Pendleton & Allamandola 2002). Starbursts often exhibit strong H<sub>2</sub>O ice absorption at 3.1 and 6.0  $\mu\text{m}$  (e.g., see Spoon et al. 2004), while these ice features are not seen in AGN where it is too hot for ice to survive against sublimation (see Li 2007). Furthermore, starbursts also emit prominently at 3.3, 6.2, 7.7, 8.6 and 11.3  $\mu\text{m}$  which are often collectively ascribed to polycyclic aromatic hydrocarbon (PAH) molecules (Léger & Puget 1984, Allamandola et al. 1985), however, these PAH emission bands are not detected in AGN (see Li 2007). The absence of PAHs in AGN is commonly attributed to the destruction of PAHs by extreme UV and soft X-ray photons in AGN (Roche et al. 1991; Voit 1991, 1992; Siebenmorgen et al. 2004).

In starbursts, the 9.7 and 18  $\mu\text{m}$  silicate features are always seen in *absorption*. In AGN, in contrast, the silicate features can be seen either in *absorption* or in *emission*, or can not be made out at all in the continuum. AGN are thought to be surrounded by an optically thick dust torus which would block the photons from the broad line region and accretion disk if they are viewed edge-on, through the torus (“type 2”), or would allow the detection of broad emission lines if they are viewed face-on (“type 1”). The anisotropic torus is invoked by the unification theory of AGN to account for the observational dichotomy (Antonucci 1993; Urry & Padovani 1995). In type 1 AGN, silicates are expected to *emit* at 9.7 and 18  $\mu\text{m}$  where

hot dust can be directly detected, while in type 2 AGN, silicates are expected to be seen in *absorption* because of torus obscuration (see Li 2007, Mason 2015).<sup>1</sup> Moreover, starbursts show a *steeply rising* emission continuum at  $\sim 5\text{--}8\ \mu\text{m}$  before the onset of the  $9.7\ \mu\text{m}$  silicate feature, while the  $\sim 5\text{--}8\ \mu\text{m}$  emission continuum is *flat* in AGN.

Very recently, Xie et al. (2014) studied the  $\sim 5\text{--}40\ \mu\text{m}$  infrared (IR) spectra of IRAS F10398+1455, IRAS F21013-0739, and SDSS J0808+3948 obtained with the *Infrared Spectrograph* (IRS) on board the *Spitzer Space Telescope* (Houck et al. 2004). They found that the IR spectra of these galaxies are *anomalous*. Spectroscopically, on one hand they resemble that of AGN in the sense that the silicate features in these galaxies are seen in *emission*; however, they also exhibit strong PAH emission features which are absent in AGN. On the other hand, they are like starbursts in the sense that the  $\sim 5\text{--}8\ \mu\text{m}$  emission continua of both these galaxies and starbursts all steeply rise with wavelength  $\lambda$  and they all show strong PAH emission features. However, the silicate features seen in *emission* in these galaxies are often seen in *absorption* in starbursts. Furthermore, the *steep*  $\sim 5\text{--}8\ \mu\text{m}$  emission continuum seen in these galaxies is much *flatter* in AGN (see Figure 1 of Xie et al. 2014). Let  $d \ln F_\nu / d \ln \lambda$  be the slope of the  $\sim 5\text{--}8\ \mu\text{m}$  emission continuum, where  $F_\nu$  is the observed flux at frequency  $\nu$ ,  $\lambda = c/\nu$  is wavelength, and  $c$  is the speed of light. On average,  $d \ln F_\nu / d \ln \lambda \approx 0.8$  for AGN, while for IRAS F10398+1455, IRAS F21013-0739, and SDSS J0808+3948,  $d \ln F_\nu / d \ln \lambda \approx 4.1, 4.2$ , and  $4.6$ , respectively. A detailed description of the spectral properties and a comparison of the *Spitzer*/IRS spectra of these three galaxies with that of typical starbursts and quasars can be found in Xie et al. (2014).

The focus of this paper is to explore the unique properties of the dust in terms of composition, size and temperature in these three spectroscopically anomalous galaxies. This paper is organized as follows. We describe the data in §2. In §3 we describe the dust model and calculate the mass absorption coefficients of various silicate and carbon dust species in the IR. The model-fitting to the observed IR emission is presented in §4. In §5 we compare the PAHFIT approach with the spline approach, and also compare the IR emission of our three galaxies with that of quasars and IRAS FSC10214+4724, an ultraluminous IR galaxy (ULIRG). The major conclusions are summarized in §6. Throughout the paper, we assume a cosmological model with  $H_0 = 70\ h_{70}\ \text{km s}^{-1}\ \text{Mpc}^{-1}$ ,  $\Omega_m = 0.3$  and  $\Omega_\Lambda = 0.7$ . The  $L_\odot$  represents solar luminosity of  $3.826 \times 10^{33}\ \text{ergs s}^{-1}$  and  $M_\odot$  represents solar mass of  $1.989 \times 10^{33}\ \text{g}$ .

---

<sup>1</sup>There are some exceptions: some type 2 AGN exhibit silicate features in *emission* instead of *absorption* (Sturm et al. 2006; Mason et al. 2009; Nikutta et al. 2009).

## 2. Observations and Data

These three galaxies were found when cross-matching the *Sloan Digital Sky Survey* (SDSS) and *Spitzer*/IRS low resolution spectra (L. Hao et al. 2015, in preparation). The *Spitzer*/IRS spectra of these galaxies are taken from the *Cornell AtlaS of Spitzer/IRS Sources* (CASSIS) which includes  $\sim 13,000$  low resolution spectra of  $>11,000$  distinct sources observed in the standard staring mode and provides publishable quality spectra (Lebouteiller et al. 2011; L. Hao et al. 2015, in preparation). We tabulate their basic properties in Table 1.

While the  $\sim 5\text{--}8\,\mu\text{m}$  continuum and the  $9.7$  and  $18\,\mu\text{m}$  silicate emission features result from dust grains which, heated by the AGN central engine, attain an equilibrium temperature (see Li 2007), the PAH emission features arise from PAH molecules which are stochastically heated by single stellar photons from their host galaxies (see Draine & Li 2001). Due to the differences in their emission mechanisms, carriers, and emitting regions, to facilitate a detailed examination of the dust emission, we first remove the PAH emission features and the ionic emission lines from the *Spitzer*/IRS spectra of these galaxies. This requires an estimation of the dust emission continuum underneath the PAH and ionic emission lines. We take two approaches in defining the continuum. First, we approximate the continuum as a sum of starlight and blackbodies of different temperatures using a modified version of the PAHFIT software (Smith et al. 2007). The continuum determined in this way is hereafter referred to as “the PAHFIT continuum.” We also define a “spline continuum” which is obtained by selecting anchor points at  $5\text{--}7$ ,  $14.5\text{--}15.0$  and  $29\text{--}30\,\mu\text{m}$  of each *Spitzer*/IRS spectrum to form a underlying continuum and then fitting these points with a spline function (L. Hao et al. 2015 in preparation). In both approaches, the PAH emission features are fitted with a number of Drude profiles which are expected for classical damped harmonic oscillators (see Li 2009), while the ionic lines are fitted with Gaussian profiles.

We are mostly interested in the “residual” dust emission obtained by subtracting the PAH and ionic emission lines from the observed *Spitzer*/IRS spectra. For illustration, we show in Figure 1 the “residual” dust emission of IRAS F10398+1455, IRAS F21013-0739 and SDSS J0808+3948 obtained by subtracting the PAH and ionic emission lines determined from the PAHFIT approach. We also show in Figure 1 the “residual” dust emission of three galaxies obtained with the spline approach. For F10398+1455, the overall “residual” dust emission profiles resulting from these two approaches are in close agreement with each other, except that the  $9.7\,\mu\text{m}$  silicate emission feature determined from the PAHFIT method is somewhat narrower than that from the spline method. In specific, the fluxes in the blue and red wings of the  $9.7\,\mu\text{m}$  silicate emission feature resulting from the PAHFIT method are lower by  $\lesssim 5\%$  than that from the spline method. The flux differences between that derived from the spline method and that from PAHFIT are more pronounced in F21013-0739

Table 1. Basic Parameters for the Three Spectroscopically Anomalous Galaxies IRAS F10398+1455, IRAS F21013-0739 and SDSS J0808+3948

Sources	R.A.	Decl.	Redshift	Classification <sup>a</sup>	Program ID <sup>b</sup>	$M_*$ <sup>c</sup> ( $M_\odot$ )	$L_{\text{IR}}$ <sup>d</sup> ( $L_\odot$ )
IRAS F10398 + 1455	10h42m33.32s	+14d39m54.1s	0.099	AGN+SB	40991	$10^{10.7}$	$10^{10.50}$
IRAS F21013 – 0739	21h03m58.75s	-07d28m02.5s	0.136	AGN+SB	40444	$10^{10.9}$	$10^{10.53}$
SDSS J0808 + 3948	08h08m44.27s	39d48m52.36s	0.091	AGN+SB	40444	$10^{9.8}$	$10^{10.84}$

<sup>a</sup>The optical classification was based on the Baldwin, Phillips & Terlevich (1981; BPT) diagram which plots the emission line ratio of  $[\text{O III}]/\text{H}\beta$  against  $[\text{N II}]/\text{H}\alpha$  (Y. Xie et al. 2015, in preparation). These three galaxies are classified as a composite of type 2 AGN and starburst.

<sup>b</sup>The program ID from which the *Spitzer*/IRS spectra were taken.

<sup>c</sup>Stellar mass (taken from the MPA-JHU SDSS DR7 catalog).

<sup>d</sup>Infrared luminosity.

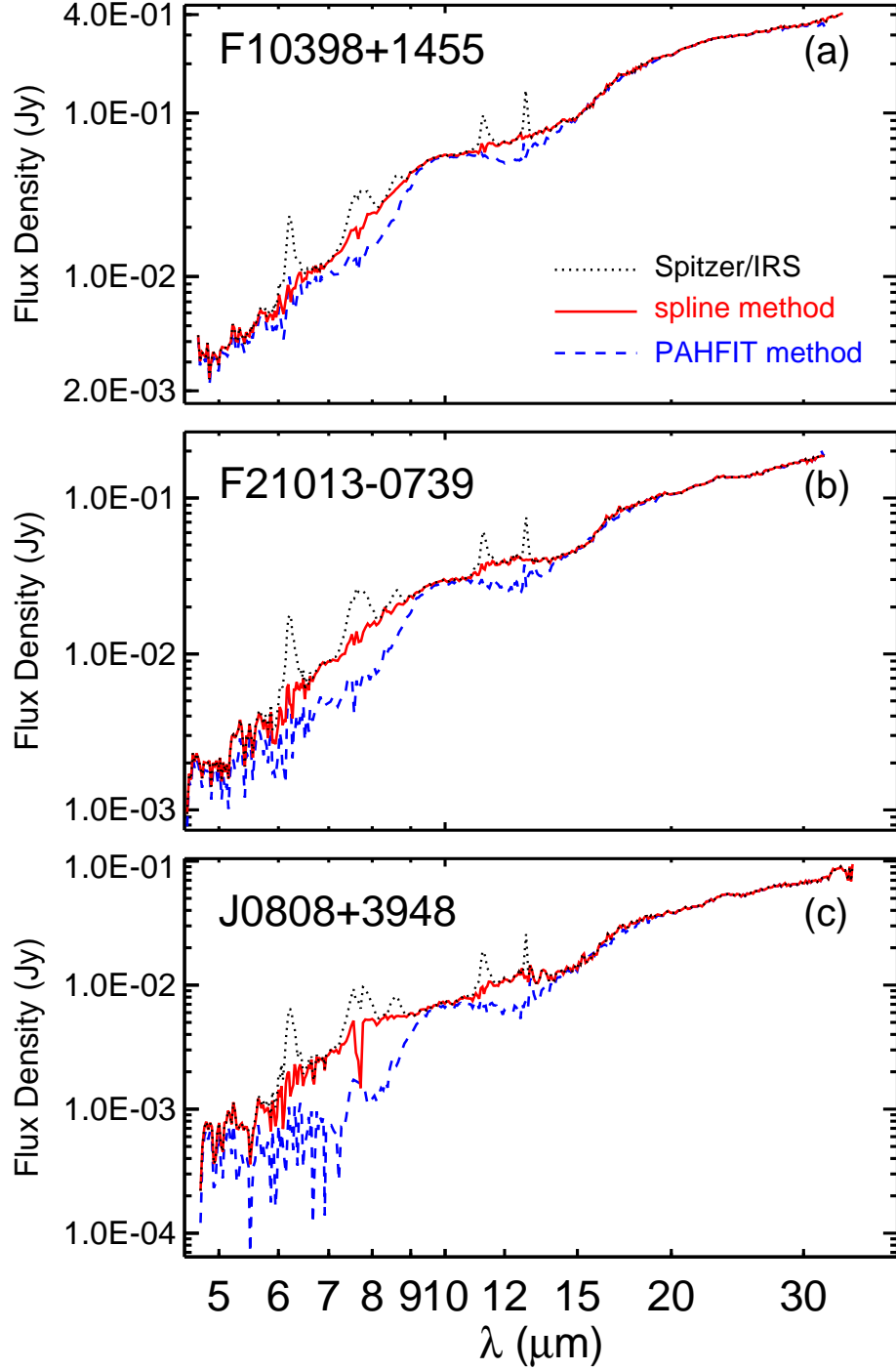


Fig. 1.— The “residual” dust emission of IRAS F10398+1455 (a), IRAS F21013-0739 (b) and SDSS J0808+3948(c) obtained by subtracting from the *Spitzer*/IRS spectrum (black dotted line) the PAH and ionic emission lines determined from the spline approach (red solid line) or from the PAHFIT approach (blue dashed line). In the spline approach, the continuum underneath the PAH emission features is fitted with a spline function. In the PAHFIT approach, the continuum underneath the PAH emission features is approximated as a sum of starlight and blackbodies of different temperatures derived from the PAHFIT software of Smith et al. (2007).

and SDSS J0808+3948 than F10398+1455, with the spline-based  $9.7\ \mu\text{m}$  emission feature being broader and less prominent.<sup>2</sup> With  $d \ln F_\nu / d \ln \lambda \approx 2.7$  and  $2.6$  for F21013-0739 and SDSS J0808+3948 respectively, the PAHFIT method results in a less steep  $\sim 5\text{--}8\ \mu\text{m}$  continuum, but still much steeper than that of AGN ( $d \ln F_\nu / d \ln \lambda \approx 0.8$ ). The relatively high flux density drawn from the spline approach could be due to an incomplete subtraction of the PAH wings. We will discuss in §5.1 the differences in our modeling results derived from the two residual spectra.

### 3. Dust Model

To model the dust emission, we need to specify the dust chemical composition, size, and temperature. For dust composition, we will consider amorphous silicate and graphite or amorphous carbon, although other dust species (e.g., SiC, oxides) may be present in AGN tori (e.g., see Laor & Draine 1993, Markwick-Kemper et al. 2007, Köher & Li 2010).

In the Milky Way diffuse ISM the dust grain sizes range from a few Angstroms to a few tenth micrometers (see Li 2004a). In AGN the dust is expected to be skewed toward a larger average grain size due to the preferential destruction of small dust in the harsh environments of AGN (see Li 2007), and probably also because of grain growth in the dense circumnuclear regions (see Maiolino et al. 2001). For simplicity, we will not consider size distributions, instead, we will only consider seven discrete sizes:  $a = 0.1, 0.5, 1.0, 1.5, 2.0, 5.0$  and  $10.0\ \mu\text{m}$  where  $a$  is the radius of the dust grains (assumed spherical). The dust sizes considered here are broad enough to cover both sub- $\mu\text{m}$ -sized dust typical of the Galactic diffuse ISM (see Li 2004a) and large,  $\mu\text{m}$ -sized dust typical of AGN (e.g., see Li et al. 2008, Smith et al. 2010, Lyu et al. 2014, Z. Shao et al. 2015, in preparation).

The dust in AGN tori is expected to have a range of temperatures. In the inner “wall” region of the torus, the dust temperature reaches  $\gtrsim 1500\ \text{K}$ , the sublimation temperature of silicate and graphite materials. The dust temperature decreases when moving away from the inner “wall.” To fully account for the temperature distribution, we need to perform radiative transfer calculations for the dust in AGN tori heated by the central engine. For simplicity, we will only consider two temperatures — a warm component and a cold component — to represent the temperature distribution.

---

<sup>2</sup>We note that, although the spline-based  $9.7\ \mu\text{m}$  silicate emission feature of SDSS J0808+3948 is almost too weak to be noticeable, the  $18\ \mu\text{m}$  O–Si–O silicate bending feature is clearly seen (see Figure 2 of Xie et al. 2014).

We assume that the observed IR emission results from silicate dust and carbon dust (i.e., graphite or amorphous carbon). For each dust species, we consider a warm component with temperature  $T_w$  and a cold component with temperature  $T_c$ . Assuming the torus is optically thin in the IR, we model the dust IR emission as

$$F_\nu = \frac{1}{d^2} \times \sum_i \{ B_\nu(T_{w,i}) \times \kappa_{\text{abs},i}(\nu) \times M_{w,i} + B_\nu(T_{c,i}) \times \kappa_{\text{abs},i}(\nu) \times M_{c,i} \} \quad , \quad (1)$$

where the sum is over the two dust species (silicate and graphite or amorphous carbon),  $d$  is the luminosity distance of the object,  $\kappa_{\text{abs},i}(\nu)$  is the mass absorption coefficient or opacity (in unit of  $\text{cm}^2 \text{g}^{-1}$ ) of dust of type  $i$ ,  $B_\nu(T)$  is the Planck function of temperature  $T$  at frequency  $\nu$ ,  $T_{w,i}$  and  $T_{c,i}$  are respectively the temperatures of the warm and cold components of dust of type  $i$ , and  $M_{w,i}$  and  $M_{c,i}$  are respectively the masses of the warm and cold components of dust of type  $i$ . For a given composition and size, we calculate the mass absorption coefficient  $\kappa_{\text{abs}}(\nu)$  from Mie theory (Bohren & Huffman 1983) using the refractive index of the corresponding dust material.

To summarize, there are in total eight parameters in fitting the observed IR emission: the temperature ( $T_w^S$ ) and mass ( $M_w^S$ ) for the warm silicate component, the temperature ( $T_c^S$ ) and mass ( $M_c^S$ ) for the cold silicate component, the temperature ( $T_w^C$ ) and mass ( $M_w^C$ ) for the warm carbon dust component, and the temperature ( $T_c^C$ ) and mass ( $M_c^C$ ) for the cold carbon dust component. We obtain the best fit for each galaxy using the MPFIT code, an IDL  $\chi^2$ -minimization routine based on the Levenberg–Marquardt algorithm (Markwardt 2009).

We require the dust temperatures not to exceed the sublimation temperature ( $T_{\text{subl}} \sim 1500 \text{ K}$ ) of silicate and graphite materials. For the dust mass, we could apply the elemental abundances to constrain the mass ratio of the silicate component to the carbon dust component. Let  $[X/H]_{\text{tot}}$  be the total abundance of element  $X$  relative to  $H$ ,  $[X/H]_{\text{gas}}$  be the amount of  $X$  in the gas phase, and  $[X/H]_{\text{dust}}$  be the amount of  $X$  contained in dust. As an element will be in the gas-phase and/or locked up in the solid-phase, one naturally obtains  $[X/H]_{\text{dust}} = [X/H]_{\text{tot}} - [X/H]_{\text{gas}}$ . Let  $\mu_X$  be the atomic weight of  $X$  ( $\mu_X \approx 12, 16, 56, 24$ , and  $28$  for carbon, oxygen, iron, magnesium, and silicon). If we assume a stoichiometric composition of  $\text{Mg}_{2x}\text{Fe}_{2(1-x)}\text{SiO}_4$  for silicate (i.e., each silicon atom corresponds to four oxygen atoms), the mass ratio of the carbon dust component to the silicate component is

$$M_{\text{carb}}/M_{\text{sil}} = \frac{\mu_C \{ [C/H]_{\text{tot}} - [C/H]_{\text{gas}} \}}{\mu_{\text{Fe}} [Fe/H]_{\text{dust}} + \mu_{\text{Mg}} [Mg/H]_{\text{dust}} + \mu_{\text{Si}} [Si/H]_{\text{dust}} + 4 \times \mu_{\text{O}} [Si/H]_{\text{dust}}} \quad . \quad (2)$$

If we assume that (i) these galaxies have the solar C, Fe, Mg and Si abundances,<sup>3</sup> (ii) all Fe, Mg and Si elements are depleted in silicate dust, and (iii)  $\sim 37\%$  of the C is in the gas-phase (i.e.,  $[\text{C}/\text{H}]_{\text{gas}} \approx 100$  ppm, Sofia et al. 2011), we derive  $M_{\text{carb}}/M_{\text{sil}} \approx 0.36$ . With C atoms all depleted in dust (i.e.,  $[\text{C}/\text{H}]_{\text{gas}} = 0$  ppm), one obtains an upper limit of  $M_{\text{carb}}/M_{\text{sil}} \approx 0.57$ . A higher  $M_{\text{carb}}/M_{\text{sil}}$  ratio could be achieved if one assumes an enstatite ( $\text{MgSiO}_3$ ) composition for the silicate component:  $M_{\text{carb}}/M_{\text{sil}} \approx 0.59$  for  $[\text{C}/\text{H}]_{\text{gas}} = 100$  ppm, or  $M_{\text{carb}}/M_{\text{sil}} \approx 0.95$  for  $[\text{C}/\text{H}]_{\text{gas}} = 0$  ppm. As we have no information about the elemental abundances and depletion for these three galaxies, in the modeling we will allow the mass ratio to vary between  $0.2 < M_{\text{carb}}/M_{\text{sil}} < 2$ .

We estimate the uncertainties for the eight model parameters by performing Monte-Carlo simulations. For the *Spitzer*/IRS spectrum of each source, we assume that the flux density error statistically follows a normal distribution. The dispersion is characterized by the observed  $1\sigma$  error, composed of the statistical and systematic errors. The latter arises from the flux differences between the two nods of the *Spitzer*/IRS spectra, the sky background contamination, and the *Spitzer*/IRS pointing and flux calibration errors (Lebouteiller et al. 2011).<sup>4</sup> We generate a new “observational” spectrum through randomly sampling a point at each wavelength from the normal distribution. We then model the new spectrum and derive a set of model parameters. We conduct 100 simulations for each source as the parameters derived from 10,000 simulations only slightly differ from that derived from 100 simulations. The final model spectrum is calculated from the median values of the model parameters. The error of each parameter is derived from the standard deviation of 100 simulations.

The mass absorption coefficient or opacity  $\kappa_{\text{abs}}(\nu)$  depends on the dust size, shape, and composition through the dielectric function or index of refraction of the dust material. For graphite, we take the index of refraction of Draine & Lee (1984). For amorphous carbon, we take the index of refraction of Rouleau & Martin (1991). For silicate, we consider a range of compositions: (i) “astronomical silicates” of Draine & Lee (1984), (ii) pyroxene  $\text{Mg}_x\text{Fe}_{1-x}\text{SiO}_3$  with  $x = 0.4, 0.7, 1.0$  (Dorschner et al. 1995), and (iii) olivine  $\text{Mg}_{2x}\text{Fe}_{2(1-x)}\text{SiO}_4$  with  $x = 0.4, 0.5$  (Dorschner et al. 1995). In Figure 2, we show the mass absorption coefficient

---

<sup>3</sup> $[\text{C}/\text{H}]_{\odot} \approx 269 \pm 31$  ppm,  $[\text{Fe}/\text{H}]_{\odot} \approx 31.6 \pm 2.9$  ppm,  $[\text{Mg}/\text{H}]_{\odot} \approx 39.8 \pm 3.7$  ppm, and  $[\text{Si}/\text{H}]_{\odot} \approx 32.4 \pm 2.2$  ppm (Asplund et al. 2009).

<sup>4</sup>We note that the signal-to-noise ratio (SNR) of the *Spitzer*/IRS spectrum in the  $\sim 5\text{--}14.5\ \mu\text{m}$  wavelength interval is lower than that in the interval of  $\sim 14.5\text{--}38\ \mu\text{m}$ . This was caused by the different observational modules (i.e., the  $5\text{--}14.5\ \mu\text{m}$  *Short Low* IRS module with a slit width of  $3''.6$ , and the  $14.5\text{--}38\ \mu\text{m}$  *Long Low* IRS module with a slit width of  $11''.2$ ). To fit the  $5\text{--}8\ \mu\text{m}$  continuum emission and the  $9.7\ \mu\text{m}$  silicate emission feature, we arbitrarily increase the weights for the data points at  $5\text{--}8$  and  $8\text{--}14.5\ \mu\text{m}$  by ten and two times, respectively, compared to that at  $14.5\text{--}38\ \mu\text{m}$ .

$\kappa_{\text{abs}}(\lambda)$  of each dust species of different sizes spanning the wavelength range of 2–40  $\mu\text{m}$ .

For all silicate species, the mass absorption coefficients  $\kappa_{\text{abs}}(\lambda)$  in the 2–40  $\mu\text{m}$  wavelength range are featured by a relatively smooth continuum at  $\sim 2\text{--}8\ \mu\text{m}$  and two prominent bumps peaking around 9.7 and 18  $\mu\text{m}$ . The  $\sim 2\text{--}8\ \mu\text{m}$  continuum increases with the dust size. The 9.7 and 18  $\mu\text{m}$  features also vary with the dust size: they substantially broaden and shift to longer wavelengths for  $a \gtrsim 1.5\ \mu\text{m}$ .<sup>5</sup> For amorphous carbon and graphite, the  $\sim 2\text{--}8\ \mu\text{m}$  continuum mass absorption coefficients flatten off with increasing dust size.

The  $\sim 2\text{--}8\ \mu\text{m}$  continuum mass absorption coefficients are sensitive to the silicate composition. As illustrated in Figure 3a, for a given dust size, the  $\sim 2\text{--}8\ \mu\text{m}$  continuum opacity increases significantly with the iron fraction of the dust. In general, amorphous olivine has a higher  $\sim 2\text{--}8\ \mu\text{m}$  continuum opacity than pyroxene. We note that the dielectric functions of the Draine & Lee (1984) “astronomical” silicate were synthesized to be “dirty” so that it is absorptive in the near-UV and optical wavelength ranges and also has a high  $\sim 2\text{--}8\ \mu\text{m}$  continuum opacity. In Figure 3b, we compare the 2–40  $\mu\text{m}$  opacities of graphite and amorphous carbon. In the  $\sim 5\text{--}8\ \mu\text{m}$  wavelength range of interest here, amorphous carbon has a higher opacity than graphite.

## 4. Results

A first glance of the mass absorption coefficient  $\kappa_{\text{abs}}(\lambda)$  profiles shown in Figures 2, 3 would lead one to speculate that the steep  $\sim 5\text{--}8\ \mu\text{m}$  emission continuum observed in the three spectroscopically anomalous galaxies could be caused by silicate dust with an iron-poor pyroxene composition; and for a given composition, small, sub- $\mu\text{m}$ -sized dust may be preferred over  $\mu\text{m}$ -sized dust (see Xie et al. 2014). In this section we apply the dust model elaborated in §3 to fit the observed *Spitzer*/IRS spectra of these galaxies by extensively exploring the parameter space of eight model parameters ( $T_{\text{w}}^{\text{S}}, T_{\text{c}}^{\text{S}}, T_{\text{w}}^{\text{C}}, T_{\text{c}}^{\text{C}}, M_{\text{w}}^{\text{S}}, M_{\text{c}}^{\text{S}}, M_{\text{w}}^{\text{C}},$  and  $M_{\text{c}}^{\text{C}}$ ) and different compositions (“astronomical silicate” [DL84], pyroxene  $\text{MgSiO}_3$  [pyr0], pyroxene  $\text{Mg}_{0.7}\text{Fe}_{0.3}\text{SiO}_3$  [pyr3], pyroxene  $\text{Mg}_{0.4}\text{Fe}_{0.6}\text{SiO}_3$  [pyr6], olivine  $\text{MgFeSiO}_4$  [olv5], olivine  $\text{Mg}_{0.8}\text{Fe}_{1.2}\text{SiO}_4$  [olv6], amorphous carbon [ac], and graphite [gra]). We will focus on fitting the “observed” spectra obtained by subtracting from the *Spitzer*/IRS spectra the PAH and ionic emission lines determined with the PAHFIT method. The model fits to the “observed” spectra obtained with the spline method will be discussed in §5.1.

---

<sup>5</sup>For  $a \lesssim 0.5\ \mu\text{m}$  (and even up to  $a \lesssim 1\ \mu\text{m}$ ), the 9.7 and 18  $\mu\text{m}$  features are insensitive to the dust size since grains with  $a \lesssim 0.5\ \mu\text{m}$  satisfy the Rayleigh scattering condition of  $2\pi a/\lambda \ll 1$  at these spectral bands (Bohren & Huffman 1983).

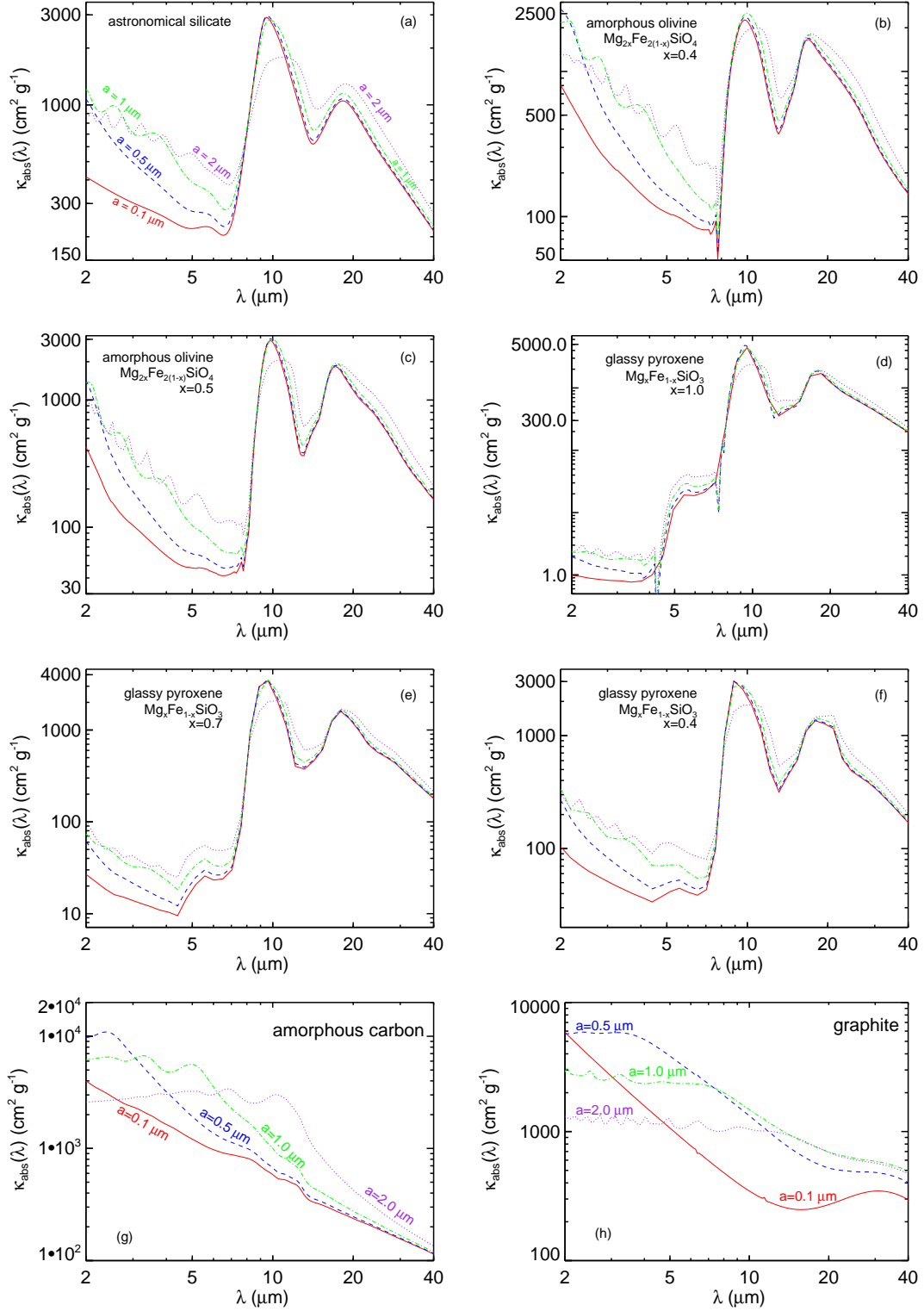


Fig. 2.— Mass absorption coefficients or opacities  $\kappa_{\text{abs}}(\lambda)$  for (a) “astronomical silicates” (Draine & Lee 1984), (b) amorphous olivine  $\text{Mg}_{0.8}\text{Fe}_{1.2}\text{SiO}_4$  (Dorschner et al. 1995), (c) amorphous olivine  $\text{MgFeSiO}_4$  (Dorschner et al. 1995), (d) glassy pyroxene  $\text{MgSiO}_3$  (Dorschner et al. 1995), (e) glassy pyroxene  $\text{Mg}_{0.7}\text{Fe}_{0.3}\text{SiO}_3$  (Dorschner et al. 1995), (f) glassy pyroxene  $\text{Mg}_{0.4}\text{Fe}_{0.6}\text{SiO}_3$  (Dorschner et al. 1995), (g) amorphous carbon (Rouleau & Martin 1991), and (h) graphite (Draine & Lee 1984). All dust species are assumed spherical with a range of radii:  $a = 0.1 \mu\text{m}$  (red solid),  $a = 0.5 \mu\text{m}$  (blue dashed),  $a = 1 \mu\text{m}$  (green dotted-dashed), and  $a = 2 \mu\text{m}$  (purple dotted).

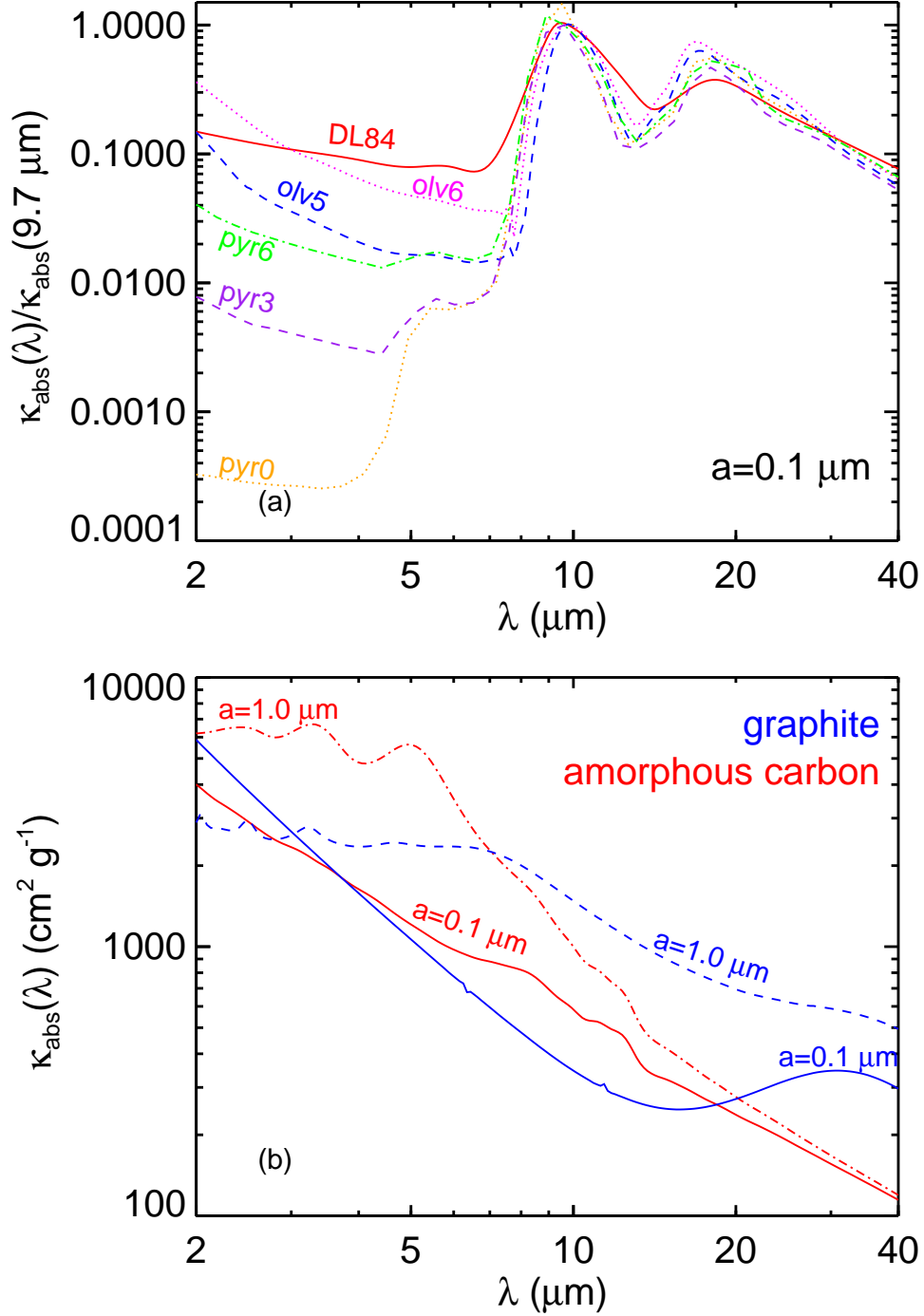


Fig. 3.— Top panel (a): comparison of the 2–40  $\mu\text{m}$  opacity of the Draine & Lee (1984) “astronomical silicate” (“DL84,” solid red) with that of pyroxene  $\text{MgSiO}_3$  (“pyr0,” dotted orange, Dorschner et al. 1995), pyroxene  $\text{Mg}_{0.7}\text{Fe}_{0.3}\text{SiO}_3$  (“pyr3,” dashed purple, Dorschner et al. 1995), pyroxene  $\text{Mg}_{0.4}\text{Fe}_{0.6}\text{SiO}_3$  (“pyr6,” dotted-dashed green, Dorschner et al. 1995), olivine  $\text{MgFeSiO}_4$  (“olv5,” dashed blue, Dorschner et al. 1995), and olivine  $\text{Mg}_{0.8}\text{Fe}_{1.2}\text{SiO}_4$  (“olv6,” dotted magenta, Dorschner et al. 1995). All silicate dust species are taken to be spherical. All dust species are assumed spherical with a radius of  $a = 0.1 \mu\text{m}$ . Bottom panel (b): comparison of the 2–40  $\mu\text{m}$  opacities of graphite (Draine & Lee 1984) of  $a = 0.1 \mu\text{m}$  (solid blue) and  $a = 1 \mu\text{m}$  (dashed blue) with that of amorphous carbon (Rouleau & Martin 1991) of  $a = 0.1 \mu\text{m}$  (solid red) and  $a = 1 \mu\text{m}$  (dotted-dashed red).

Table 2. Model Parameters for Three Spectroscopically Anomalous Galaxies (IRAS F10398+1455, IRAS F21013-0739, and SDSS J0808+3948) and Two Comparison Sources (Quasar Average Spectrum, and ULIRG IRAS FSC 10214+4724)

Object	Composition	Dust Size ( $\mu\text{m}$ )	$T_{\text{w}}^{\text{S}}$ (K)	$T_{\text{w}}^{\text{C}}$ (K)	$T_{\text{c}}^{\text{S}}$ (K)	$T_{\text{c}}^{\text{C}}$ (K)	$M_{\text{d}}^{\text{S}}$ ( $10^{34} \text{ g}$ )	$M_{\text{d}}^{\text{C}}$ ( $10^{34} \text{ g}$ )	$M_{\text{d}}^{\text{S}}$ ( $10^{37} \text{ g}$ )	$M_{\text{d}}^{\text{C}}$ ( $10^{37} \text{ g}$ )	$\chi^2/\text{dof}$
F10398+1455 <sup>a</sup>	DL84 + ac	0.1	271 $\pm$ 1.6	389 $\pm$ 2.8	92 $\pm$ 0.2	117 $\pm$ 0.1	14.0 $\pm$ 0.5	3.1 $\pm$ 0.2	5.9 $\pm$ 0.03	11.9 $\pm$ 0.07	38
F10398+1455 <sup>b</sup>	DL84 + ac	0.1	248 $\pm$ 4.9	295 $\pm$ 1.3	84 $\pm$ 0.5	115 $\pm$ 0.3	15.4 $\pm$ 2.1	27.0 $\pm$ 4.3	7.4 $\pm$ 0.08	14.8 $\pm$ 0.2	42
F10398+1455 <sup>a</sup>	olv6 + ac	0.1	303 $\pm$ 2.0	323 $\pm$ 2.2	76 $\pm$ 0.3	113 $\pm$ 0.1	8.8 $\pm$ 0.3	10.9 $\pm$ 0.5	8.7 $\pm$ 0.04	17.4 $\pm$ 0.09	25
F10398+1455 <sup>a</sup>	pyr3 + ac	1.0	248 $\pm$ 3.0	259 $\pm$ 1.5	74 $\pm$ 0.8	109 $\pm$ 0.3	16.0 $\pm$ 1.1	20.6 $\pm$ 1.9	9.1 $\pm$ 0.2	18.3 $\pm$ 0.4	24
F10398+1455 <sup>a</sup>	DL84 + gra	0.1	291 $\pm$ 4.2	319 $\pm$ 2.6	120 $\pm$ 0.6	141 $\pm$ 0.7	7.6 $\pm$ 0.5	15.2 $\pm$ 1.1	1.7 $\pm$ 0.05	2.7 $\pm$ 0.1	36
F10398+1455 <sup>a</sup>	DL84 + ac	1.0	350 $\pm$ 30.0	284 $\pm$ 3.9	93 $\pm$ 0.4	113 $\pm$ 1.1	3.7 $\pm$ 2.9	7.4 $\pm$ 6.0	6.1 $\pm$ 0.1	12.2 $\pm$ 0.2	59
F10398+1455 <sup>a</sup>	DL84 + gra	1.0	395 $\pm$ 13.8	385 $\pm$ 5.7	112 $\pm$ 0.1	121 $\pm$ 0.4	2.4 $\pm$ 0.3	1.1 $\pm$ 0.3	1.8 $\pm$ 0.02	3.1 $\pm$ 0.08	30
F10398+1455 <sup>a</sup>	olv6 + ac	1.0	346 $\pm$ 4.0	285 $\pm$ 1.6	81 $\pm$ 0.4	111 $\pm$ 0.3	4.5 $\pm$ 0.2	9.0 $\pm$ 0.4	8.0 $\pm$ 0.1	16.0 $\pm$ 0.2	30
F10398+1455 <sup>a</sup>	DL84 + ac	0.1	244 $\pm$ 3.3	357 $\pm$ 3.2	92 $\pm$ 1.0	115 $\pm$ 0	23.7 $\pm$ 2.1	5.4 $\pm$ 0.6	6.2 $\pm$ 0.2	12.5 $\pm$ 0.3	42
F10398+1455 <sup>a</sup>	DL84 + ac	1.5	410 $\pm$ 4.5	374 $\pm$ 4.1	93 $\pm$ 0.2	109 $\pm$ 0.1	2.4 $\pm$ 0.1	0.6 $\pm$ 0.05	6.2 $\pm$ 0.03	12.4 $\pm$ 0.05	99
F10398+1455 <sup>a</sup>	olv6 + ac	1.5	358 $\pm$ 13.4	354 $\pm$ 4.5	84 $\pm$ 1.1	108 $\pm$ 0.2	4.0 $\pm$ 0.5	1.3 $\pm$ 0.3	7.6 $\pm$ 0.3	15.0 $\pm$ 0.5	51
F10398+1455 <sup>a</sup>	pyr3 + ac	1.5	331 $\pm$ 3.5	385 $\pm$ 3.0	78 $\pm$ 1.6	109 $\pm$ 0.4	4.5 $\pm$ 0.2	0.9 $\pm$ 0.04	8.3 $\pm$ 0.3	16.6 $\pm$ 0.7	27
F10398+1455 <sup>a</sup>	DL84 + ac	2.0	419 $\pm$ 3.1	334 $\pm$ 3.0	99 $\pm$ 0.1	99 $\pm$ 0.1	2.8 $\pm$ 0.06	1.2 $\pm$ 0.1	6.0 $\pm$ 0.02	12.0 $\pm$ 0.04	201
F10398+1455 <sup>a</sup>	olv6 + ac	2.0	464 $\pm$ 50.0	324 $\pm$ 14.0	89 $\pm$ 0.2	99 $\pm$ 0.5	1.5 $\pm$ 1.3	2.6 $\pm$ 2.4	7.9 $\pm$ 0.1	15.8 $\pm$ 0.2	168
F10398+1455 <sup>a</sup>	pyr3 + ac	2.0	641 $\pm$ 8.4	382 $\pm$ 2.4	89 $\pm$ 0.1	102 $\pm$ 0.1	0.6 $\pm$ 0.02	1.1 $\pm$ 0.04	7.5 $\pm$ 0.02	15.0 $\pm$ 0.05	101
F21013-0731 <sup>a</sup>	DL84 + ac	0.1	249 $\pm$ 4.0	361 $\pm$ 5.0	61 $\pm$ 0.4	110 $\pm$ 0.5	24.6 $\pm$ 2.1	4.9 $\pm$ 0.4	15.0 $\pm$ 0.8	19.8 $\pm$ 1.8	18
F21013-0731 <sup>b</sup>	DL84 + ac	0.1	240 $\pm$ 0.0	301 $\pm$ 1.3	74 $\pm$ 0.8	120 $\pm$ 3.6	16.2 $\pm$ 0.5	32.5 $\pm$ 1.0	20.7 $\pm$ 4.4	10.3 $\pm$ 4.0	21
F21013-0731 <sup>a</sup>	olv6 + ac	0.1	334 $\pm$ 5.0	318 $\pm$ 4.6	58 $\pm$ 0.4	113 $\pm$ 0.6	6.3 $\pm$ 0.4	12.0 $\pm$ 0.1	49.0 $\pm$ 3.9	16.7 $\pm$ 2.5	17
F21013-0731 <sup>a</sup>	pyr3 + ac	1.0	251 $\pm$ 9.2	255 $\pm$ 3.2	66 $\pm$ 3.7	110 $\pm$ 1.1	16.4 $\pm$ 4.5	21.7 $\pm$ 6.9	26.0 $\pm$ 9.4	16.3 $\pm$ 19.3	17
F21013-0731 <sup>a</sup>	DL84 + gra	0.1	267 $\pm$ 0.5	327 $\pm$ 5.5	111 $\pm$ 0.4	144 $\pm$ 0.6	14.4 $\pm$ 0.02	12.2 $\pm$ 1.4	1.7 $\pm$ 0.003	2.6 $\pm$ 0.03	19
F21013-0731 <sup>a</sup>	DL84 + ac	0.1	270 $\pm$ 4.3	374 $\pm$ 5.3	74 $\pm$ 2.0	115 $\pm$ 0.0	15.0 $\pm$ 1.4	3.7 $\pm$ 0.6	9.7 $\pm$ 1.1	15.0 $\pm$ 2.6	20
J0808+3948 <sup>a</sup>	DL84 + ac	0.1	265 $\pm$ 55.0	363 $\pm$ 50.0	84 $\pm$ 11.7	110 $\pm$ 2.0	1.7 $\pm$ 0.9	0.3 $\pm$ 0.2	1.7 $\pm$ 0.9	2.4 $\pm$ 1.4	0.3
J0808+3948 <sup>b</sup>	DL84 + ac	0.1	200 $\pm$ 0.0	285 $\pm$ 3.5	78 $\pm$ 11.6	106 $\pm$ 2.0	3.2 $\pm$ 0.2	6.3 $\pm$ 0.5	2.1 $\pm$ 0.4	3.0 $\pm$ 0.3	0.7
J0808+3948 <sup>a</sup>	olv6 + ac	0.1	297 $\pm$ 58	383 $\pm$ 53.0	65 $\pm$ 5.9	108 $\pm$ 3.1	1.3 $\pm$ 1.0	0.3 $\pm$ 0.3	2.3 $\pm$ 1.4	3.7 $\pm$ 2.6	0.2
J0808+3948 <sup>a</sup>	pyr3 + ac	1.0	239 $\pm$ 24.5	294 $\pm$ 26.0	67 $\pm$ 5.9	105 $\pm$ 2.4	2.5 $\pm$ 1.5	0.5 $\pm$ 0.4	2.1 $\pm$ 0.7	4.1 $\pm$ 1.5	0.8
J0808+3948 <sup>a</sup>	DL84 + gra	0.1	265 $\pm$ 56.0	379 $\pm$ 66.0	106 $\pm$ 6.5	129 $\pm$ 7.4	1.7 $\pm$ 1.3	0.3 $\pm$ 0.3	0.5 $\pm$ 0.2	0.5 $\pm$ 0.3	0.5
J0808+3948 <sup>a</sup>	DL84 + ac	0.1	285 $\pm$ 34.0	384 $\pm$ 35.0	87 $\pm$ 3.6	115 $\pm$ 0.0	1.1 $\pm$ 0.5	0.2 $\pm$ 0.1	1.7 $\pm$ 0.3	1.8 $\pm$ 0.4	0.3
Quasar	DL84 + gra	1.5	350 $\pm$ 32.0	644 $\pm$ 5.8	40 $\pm$ 6.0	149 $\pm$ 1.3	–	–	–	–	0.42
FSC 10214+4724	DL84 + gra	0.5	394 $\pm$ 78	377 $\pm$ 132	72 $\pm$ 35	138 $\pm$ 11	$5.2 \times 10^3$	$2.4 \times 10^3$	$1.9 \times 10^4$	$5.6 \times 10^3$	5.8

<sup>a</sup>Model parameters derived from the PAHFIT-based IR emission.<sup>b</sup>Model parameters derived from the spline-based IR emission.

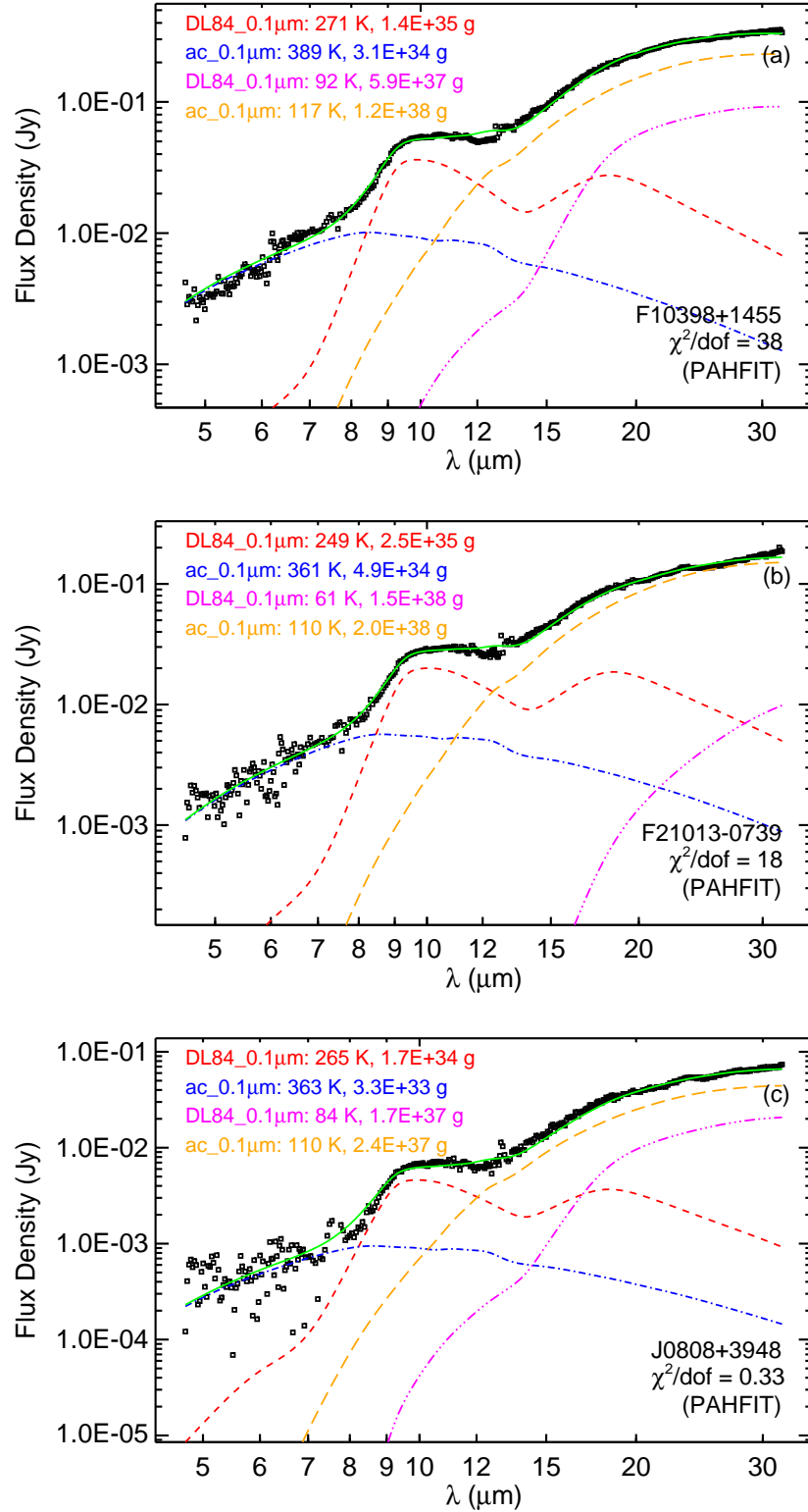


Fig. 4.— Comparison of the model emission (solid green line) of IRAS F10398+1455 (a), IRAS F21013-0739 (b), and SDSS J0808+3948 (c) with the “observed” spectra (black open squares) obtained by subtracting from the *Spitzer*/IRS spectra the PAH and ionic emission lines determined with the PAHFIT method. The model consists of four components: warm silicate (red dashed line), cold silicate (magenta dot-long dashed line), warm amorphous carbon (blue dotted–dashed line), and cold amorphous carbon (orange long dashed line). All dust components are taken to be  $0.1\,\mu\text{m}$  in radii. The DL84 “astronomical” silicate is adopted for

#### 4.1. Dust Composition

We first consider the DL84 “astronomical” silicate and amorphous carbon, and take all dust components to have the same grain size of  $0.1\,\mu\text{m}$  in radii. The effects of dust size will be discussed in §4.2. In Figure 4 we show the model fits to the “observed” spectra of IRAS F10398+1455, IRAS F21013-0739 and SDSS J0808+3948. The overall fits are very good except for SDSS J0808+3948; the model  $9.7\,\mu\text{m}$  silicate profile is a little bit too broad and its peak wavelength is a little bit too short. Also, for IRAS F10398+1455 and IRAS F21013-0739, the model slightly overpredicts the red wing of the  $9.7\,\mu\text{m}$  feature. For all three sources, the  $\sim 5\text{--}8\,\mu\text{m}$  emission continuum is dominated by warm amorphous carbon, and the emission at  $\lambda > 14\,\mu\text{m}$  is dominated by cold amorphous carbon.

We then consider models consisting of amorphous olivine and amorphous carbon. Assuming a size of  $a = 0.1\,\mu\text{m}$  for all dust components, we find that  $\text{Mg}_{0.8}\text{Fe}_{1.2}\text{SiO}_4$  (together with amorphous carbon) provides an excellent fit to all three sources (see Figure 5). Similarly, we have also considered models consisting of amorphous pyroxene and amorphous carbon. As shown in Figure 6, excellent fits are achieved with  $\text{Mg}_{0.7}\text{Fe}_{0.3}\text{SiO}_3$  of  $a = 1.0\,\mu\text{m}$ . This is because the  $9.7\,\mu\text{m}$  feature of pyroxene dust is appreciably narrower than that of amorphous olivine and “astronomical” silicate (see Figure 3). Therefore, models consisting of  $a = 0.1\,\mu\text{m}$  pyroxene and amorphous carbon produce too narrow a  $9.7\,\mu\text{m}$  feature. On the other hand, if the dust is too large (say,  $a = 2.0\,\mu\text{m}$ ), the model  $9.7\,\mu\text{m}$  feature will be too broad to be consistent with the observed spectra (see §4.2).

We have also considered graphite. As shown in Figure 7, models consisting of graphite and “astronomical silicate” of  $a = 0.1\,\mu\text{m}$  closely fit the observed IR emission of all three galaxies, with the fitting  $\chi^2$  at a similar level as that of the “astronomical silicate”/amorphous carbon model (see Figure 4).

#### 4.2. Dust Sizes

Xie et al. (2014) speculated that the steep  $\sim 5\text{--}8\,\mu\text{m}$  emission continuum seen in these spectroscopically anomalous galaxies could arise from sub- $\mu\text{m}$ -sized silicate dust instead of  $\mu\text{m}$ -sized silicate dust since the latter displays a larger opacity in the  $\sim 5\text{--}8\,\mu\text{m}$  wavelength range (see Figure 2). However, as demonstrated in §4.1, the  $\sim 5\text{--}8\,\mu\text{m}$  emission continuum is dominated by the carbon dust component. Therefore, the  $\sim 5\text{--}8\,\mu\text{m}$  continuum is not a powerful constraint on the silicate dust grain size. Instead, the  $9.7\,\mu\text{m}$  feature allows us to place a stronger constraint. Indeed, as shown in Figures 8–10, for models consisting of different silicate and carbon dust species (“astronomical silicate,” olivine, pyroxene, graphite,

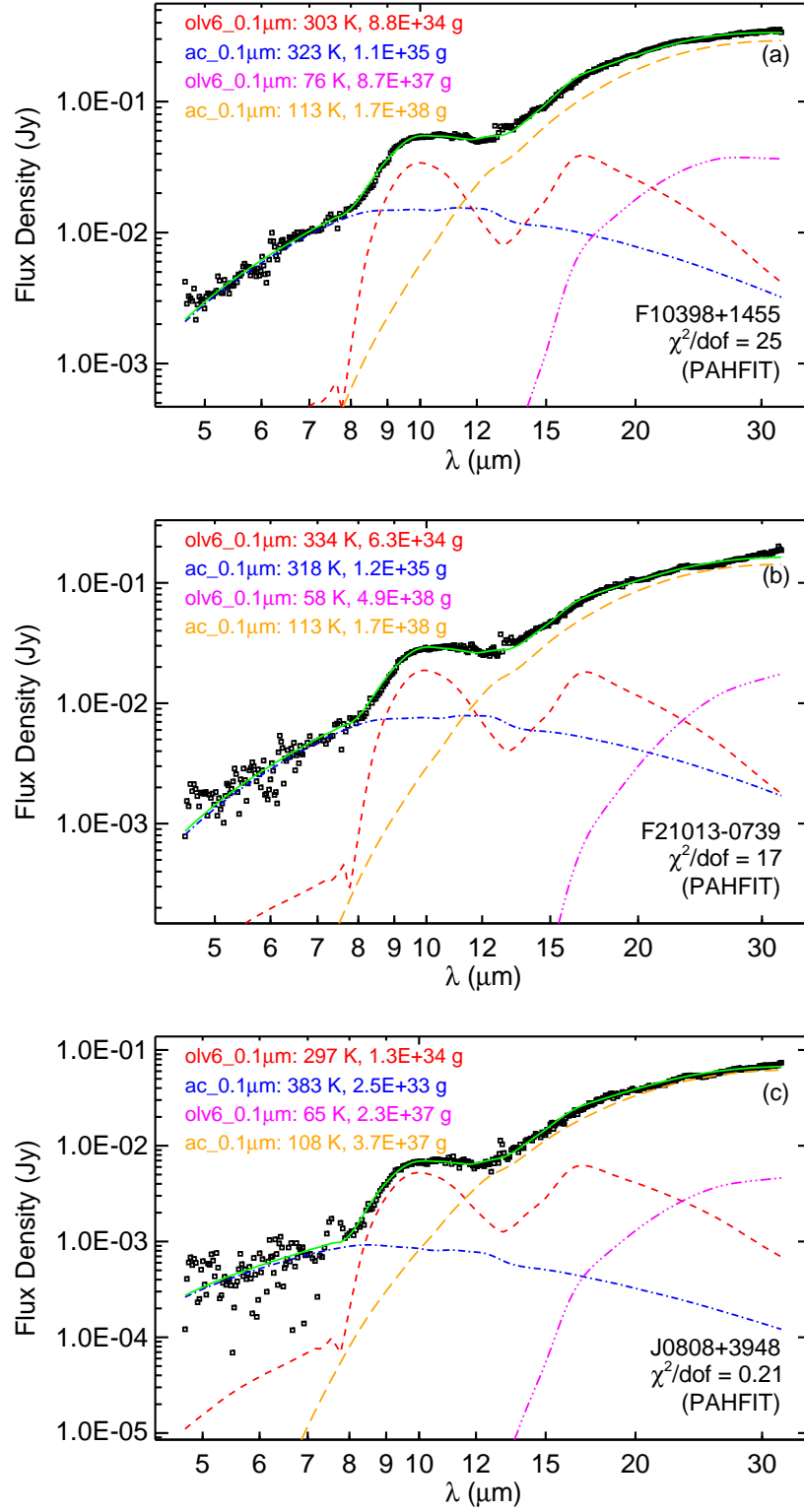


Fig. 5.— Same as Figure 4 but with the DL84 “astronomical silicate” replaced by amorphous olivine  $\text{Mg}_{0.8}\text{Fe}_{1.2}\text{SiO}_4$  (“olv6”).

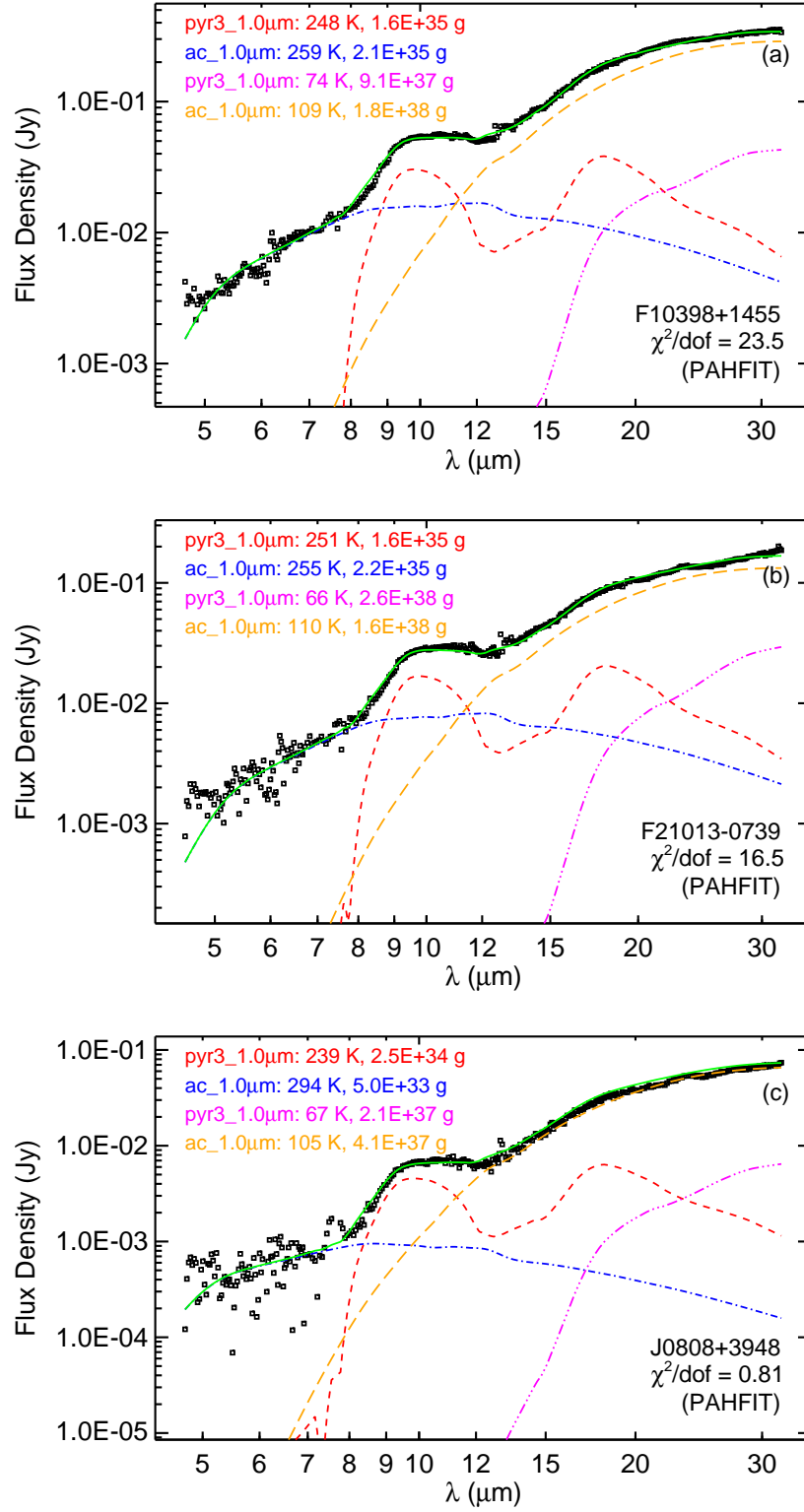


Fig. 6.— Same as Figure 4 but with the DL84 “astronomical silicate” replaced by amorphous pyroxene  $\text{Mg}_{0.7}\text{Fe}_{0.3}\text{SiO}_3$  (“pyr3”) and all dust components taken to have a size of  $a = 1.0 \mu\text{m}$ .

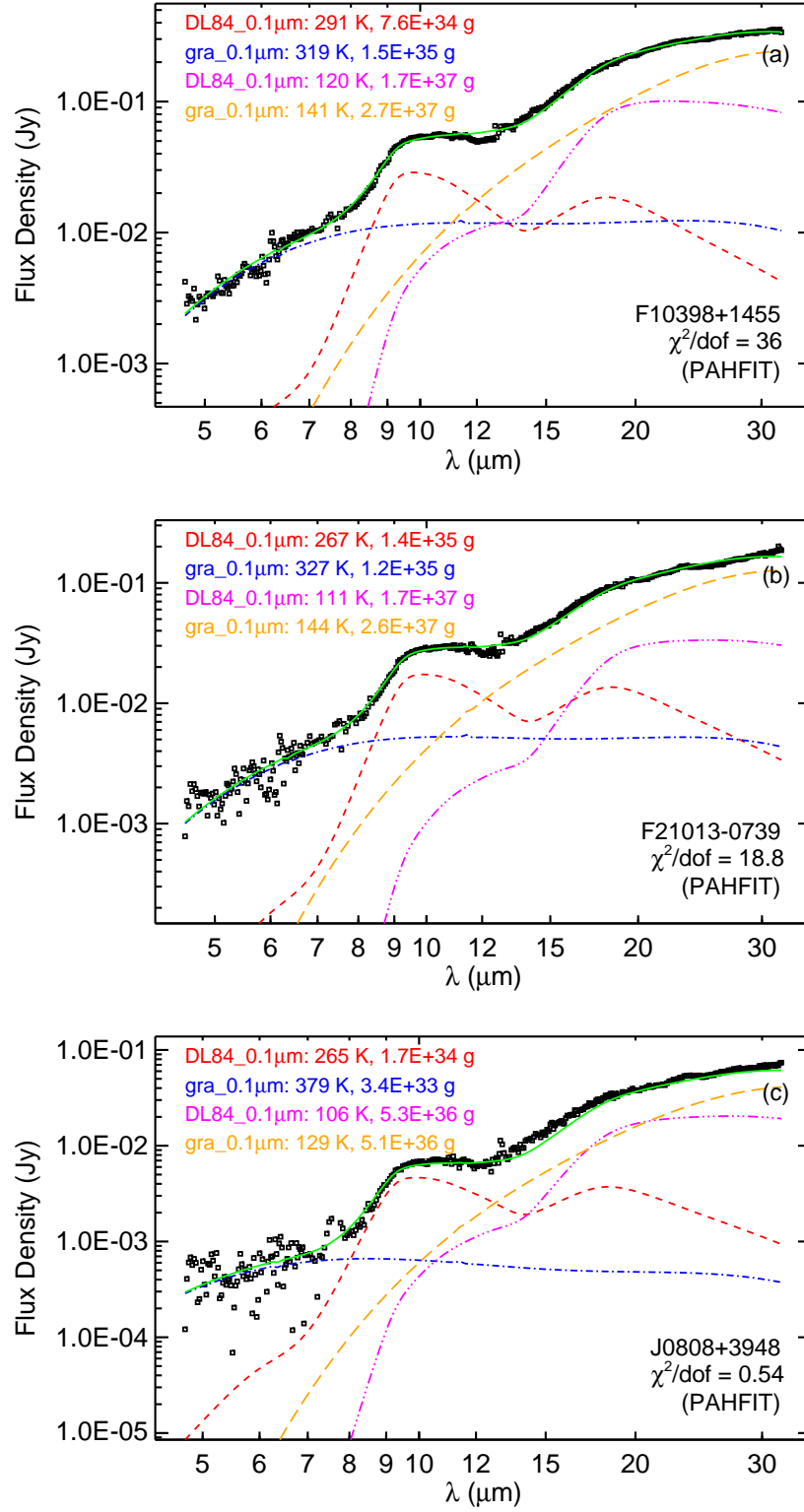


Fig. 7.— Same as Figure 4 but with the amorphous carbon component replaced by graphite.

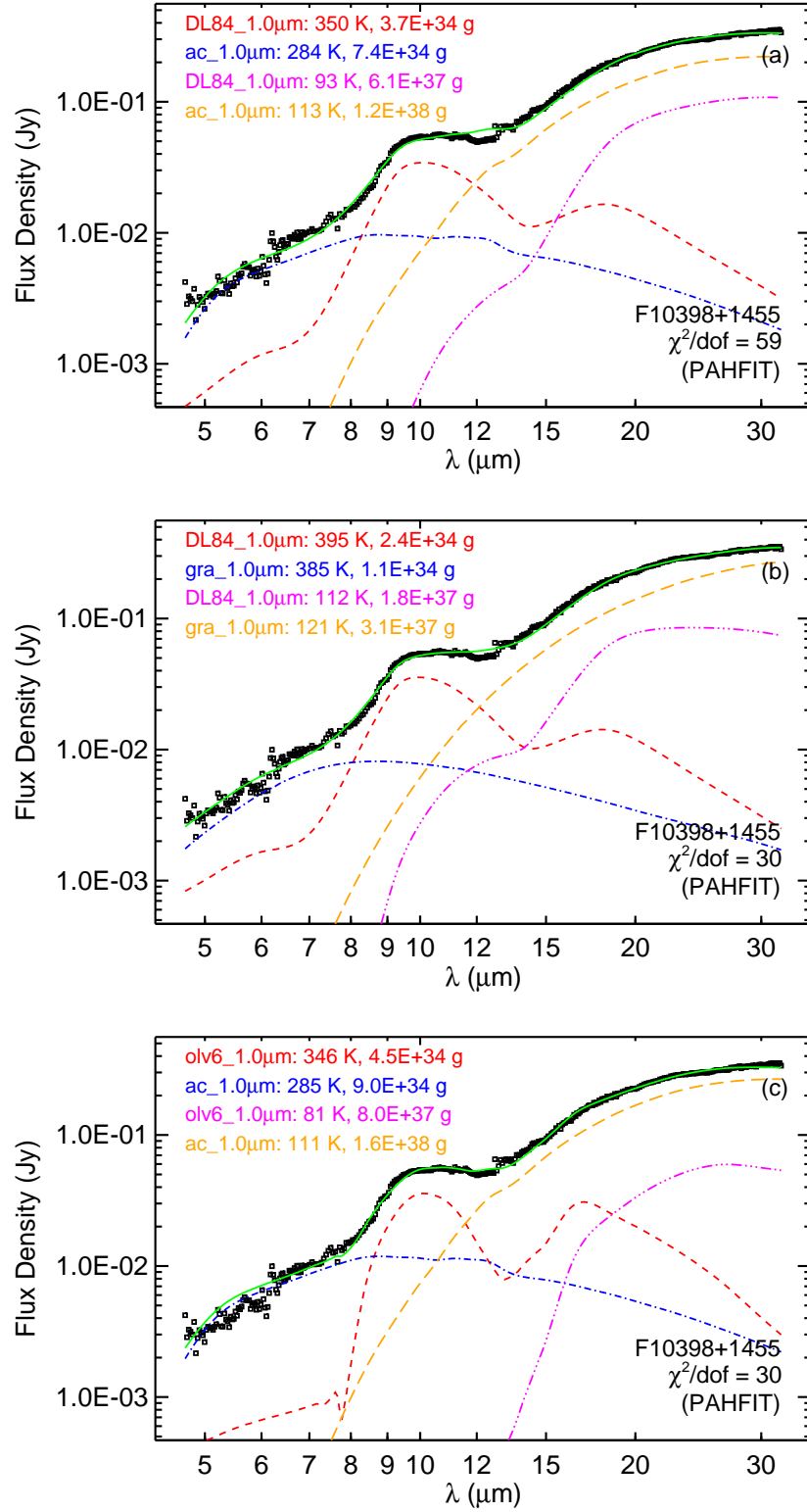


Fig. 8.— Upper panel (a): Same as Figure 4(a) but with  $a = 1.0\mu\text{m}$  for all dust components. Middle panel (b): Same as Figure 7(a) but with  $a = 1.0\mu\text{m}$  for all dust components. Bottom panel (c): Same as Figure 5(a) but with  $a = 1.0\mu\text{m}$  for all dust components.

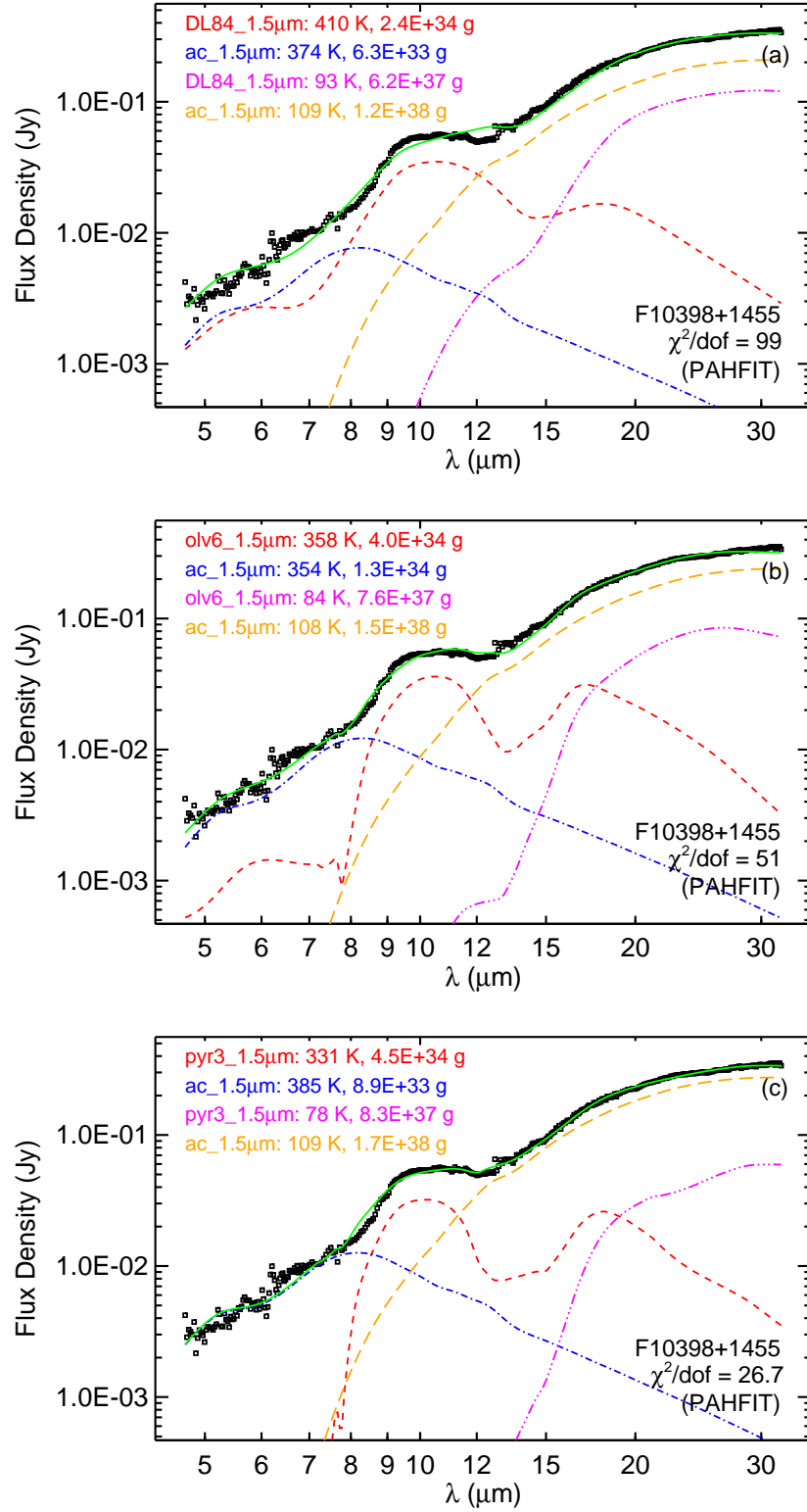


Fig. 9.— Upper panel (a): same as Figure 4(a) but with  $a = 1.5 \mu\text{m}$  for all dust components. Middle panel (b): same as Figure 5(a) but with  $a = 1.5 \mu\text{m}$  for all dust components. Bottom panel (c): same as Figure 6(a) but with  $a = 1.5 \mu\text{m}$  for all dust components.

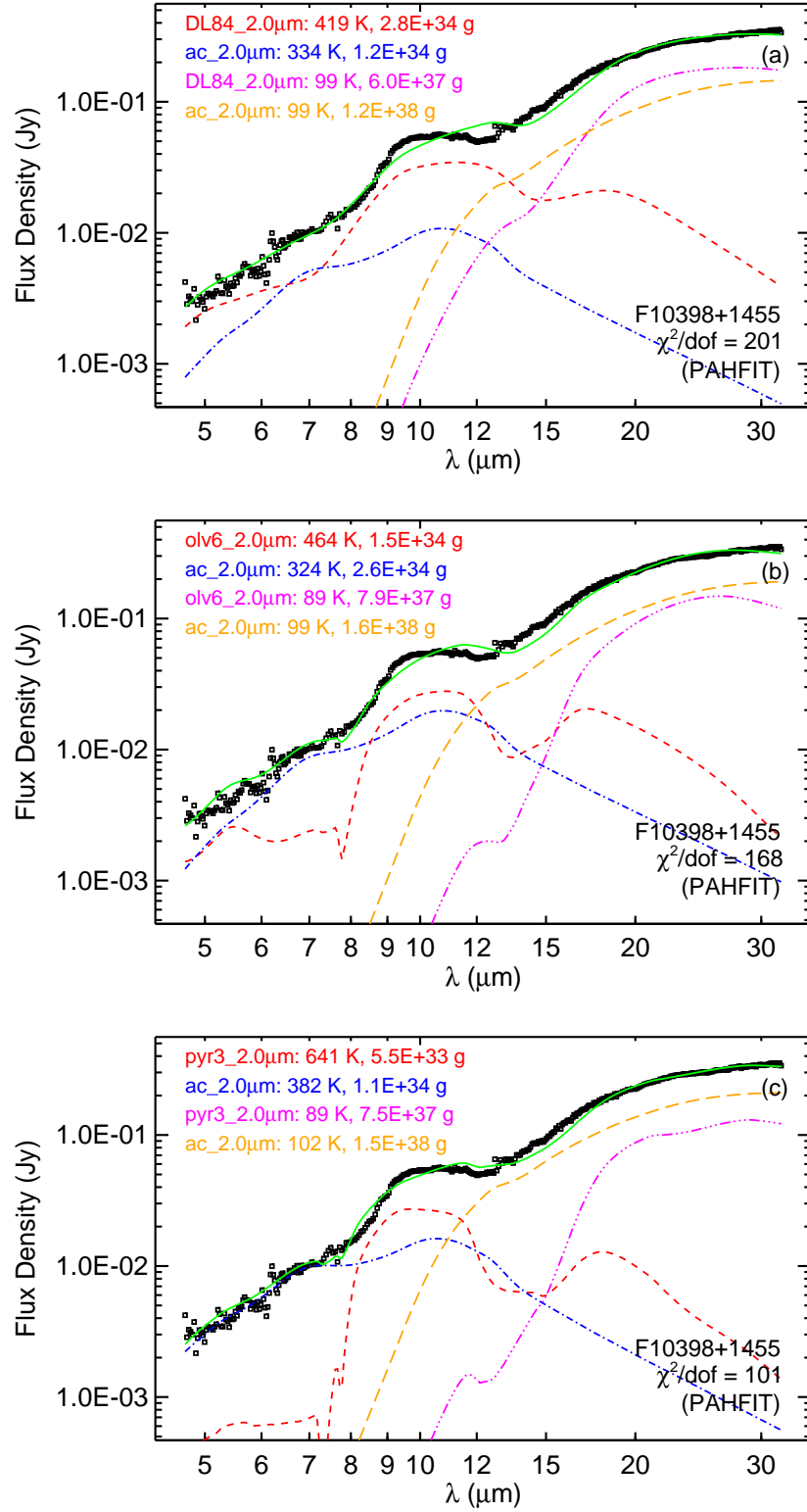


Fig. 10.— Same as Figure 9 but with  $a = 2.0 \mu\text{m}$  for all dust components.

and amorphous carbon), the observed IR emission could still be closely fitted with  $a = 1.0 \mu\text{m}$ , but not with  $a = 1.5 \mu\text{m}$  or  $a = 2.0 \mu\text{m}$ . This is easy to understand: as illustrated in Figure 2, the  $9.7 \mu\text{m}$  profile is insensitive to dust size for  $a \lesssim 1 \mu\text{m}$ , but it considerably broadens for larger sizes. The best-fit models with  $a = 1.0 \mu\text{m}$  lead to an appreciably higher temperature for the warm silicate component ( $T_{\text{w}}^{\text{S}}$ ) compared with that of the best-fit models with  $a = 0.1 \mu\text{m}$ . Consequently, the mass required by the warm silicate component ( $M_{\text{w}}^{\text{S}}$ ) drops by a factor of  $\sim 3$ – $5$ . This can be understood in the sense that, compared with silicate dust of  $a = 0.1 \mu\text{m}$ , the “ $9.7 \mu\text{m}$ ” silicate feature of the opacity  $\kappa_{\text{abs}}(\nu)$  profile of silicate dust of  $a = 1.0 \mu\text{m}$  slightly shifts to a longer wavelength. To compensate this “redshift,” one requires an increased temperature which blueshifts the peak wavelength of the Planck function  $B_{\nu}(T)$ , and therefore the resulting emission spectrum which is the product of  $B_{\nu}(T)$  and  $\kappa_{\text{abs}}(\nu)$  remains at the observed peak wavelength. The effects of grain size on the derived dust temperature are manifested in Figures 9 and 10.

## 5. Discussion

We have shown in §4 that a simple model consisting of four dust components (warm and cold silicate dust, and warm and cold carbon dust) closely reproduces the observed IR emission of all three spectroscopically anomalous galaxies, including the steeply rising  $\sim 5$ – $8 \mu\text{m}$  emission continuum and the  $9.7 \mu\text{m}$  emission feature. The model-fitting results are insensitive to the exact silicate or carbonaceous dust composition. As shown in Figures 4–7, models consisting of “astronomical” silicate, amorphous olivine, or pyroxene, combined with amorphous carbon or graphite, are all capable of successfully fitting the observed IR emission. The  $\sim 5$ – $8 \mu\text{m}$  emission continuum is dominated by the warm carbon dust component with  $T$  in the range of  $\sim 250$ – $400$  K. The  $9.7 \mu\text{m}$  silicate emission is predominantly due to silicate dust of  $T \sim 200$ – $400$  K. The emission at  $\lambda > 14 \mu\text{m}$  is dominated by the cold carbon dust component mostly with  $T \sim 110$ – $120$  K. The  $9.7 \mu\text{m}$  emission feature constrains the silicate dust size to not exceed  $\sim 1.0 \mu\text{m}$  (i.e.,  $a \lesssim 1.0 \mu\text{m}$ , see Figures 8–10). The mass ratio of the warm carbon dust to the warm silicate dust ( $M_{\text{w}}^{\text{S}}/M_{\text{w}}^{\text{C}}$ ) ranges from  $\sim 0.2$  to  $\sim 2.0$ , with a mean ratio of  $\sim 0.98$ . Similarly, the mass ratio of the cold carbon dust to the cold silicate dust ( $M_{\text{c}}^{\text{S}}/M_{\text{c}}^{\text{C}}$ ) ranges from  $\sim 0.34$  to  $\sim 2.0$ , with a mean ratio of  $\sim 1.5$ . The total dust mass is dominated by the cold components, with the warm components only accounting for  $< 0.15\%$  of the total dust mass.

To investigate the significance of the dust temperature and mass yielded from our dust IR emission modeling, for all three sources we fix the temperature of the cold carbon dust component to be  $T_{\text{c}}^{\text{C}} = 115$  K and then probe the dust temperature and mass variations for

the other components. Figure 11 shows the model spectra for all three sources obtained from the mixture of “astronomical silicate” and amorphous carbon (“DL84 + ac”) with  $a = 0.1 \mu\text{m}$  and  $T_c^C = 115 \text{ K}$ . The model spectra are in close agreement with the observed spectra. Compared with the same model but with  $T_c^C$  treated as a free parameter (see Figure 4), the temperatures derived for the other three components ( $T_w^S$ ,  $T_w^C$ , and  $T_c^S$ ) vary within  $< 10\%$ , while the derived masses ( $M_w^S$ ,  $M_w^C$ , and  $M_c^S$ ) vary within  $< 75\%$ .

To test the reasonableness of the dust mass derived in §4, for each source we compare the dust mass with the stellar mass. On average, the dust-to-stellar mass ratio of these three galaxies is  $\sim 10^{-5}$ , much smaller than that of the Milky Way ( $\sim 10^{-3}$ ; see Li 2004b). This ratio appears reasonable since the mid-IR emission considered here only probes the dust of  $T > 100 \text{ K}$  (see Table 2), while the bulk dust mass is in dust with  $T < 100 \text{ K}$  in the host galaxy which emits in the far-IR and escapes from detection by *Spitzer*/IRS.

### 5.1. PAHFIT Versus Spline

The results presented in §4 are derived by fitting the “observed” IR emission obtained by subtracting from the *Spitzer*/IRS spectra the PAH and ionic emission lines determined with the PAHFIT method. As illustrated in Figure 1, the IR emission spectra derived from the spline method show a relatively broad and weak  $9.7 \mu\text{m}$  silicate emission feature in comparison with that from PAHFIT. Furthermore, the spline method yields a steeper slope for the  $\sim 5\text{--}8 \mu\text{m}$  continuum than PAHFIT (see §2). We have also modeled the spline-based “observed” IR emission of all three spectroscopically anomalous galaxies. As illustrated in Figure 12, the simple four-component model consisting of warm/cold silicate dust and warm/cold carbon dust closely reproduces the “observed” IR emission obtained from the spline method. The temperatures and masses of the cold components for all sources do not change much ( $< 10\%$  for  $T$ , and  $< 30\%$  for  $M$ ; see Table 2) since the PAHFIT- and spline-based IR emission spectra exhibit little difference beyond  $\lambda \sim 14 \mu\text{m}$  where the cold components dominate the radiation. In contrast, the temperature of the warm silicate component derived from the spline method drops by  $\sim 10\text{--}25\%$  and its mass changes by a factor of  $\sim 1.1\text{--}1.9$ . For the warm carbon component, on average, its temperature drops by  $\sim 20\%$ <sup>6</sup> and the corresponding mass increases by a factor of  $\sim 8.7$ ,  $\sim 6.6$  and  $\sim 21$  for F10398+1455, F21013-0739 and SDSS J0808+3948, respectively.

---

<sup>6</sup>Compared with PAHFIT, the spline method yields a steeper and higher  $\sim 5\text{--}8 \mu\text{m}$  continuum (see Figure 1) and therefore a lower temperature and larger mass for the warm carbon component which dominates the  $\sim 5\text{--}8 \mu\text{m}$  continuum.

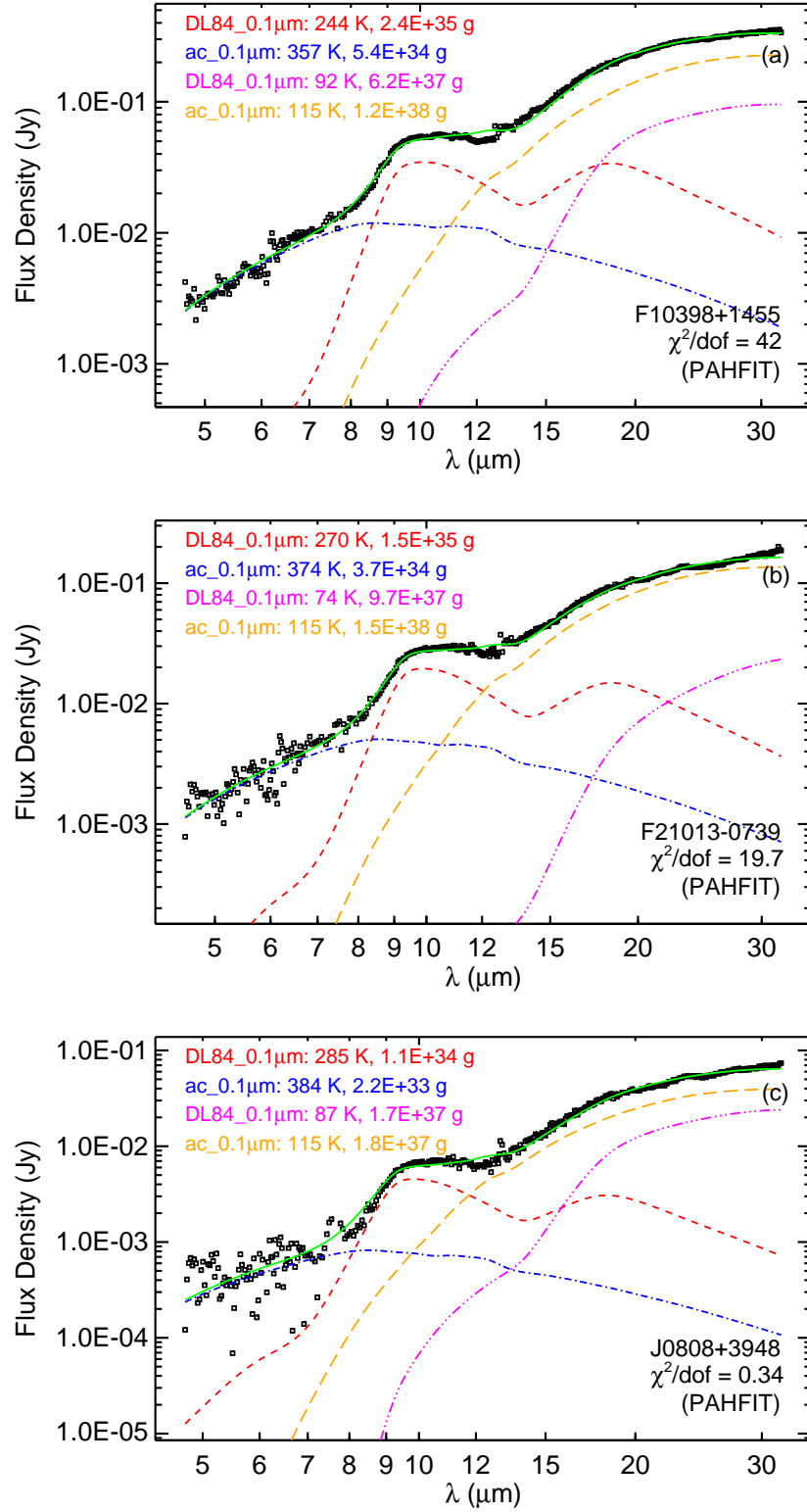


Fig. 11.— Same as Figure 4 but with the temperature of the cold carbon component (orange long dashed line) fixed at  $T_c^C = 115$  K (see §5).

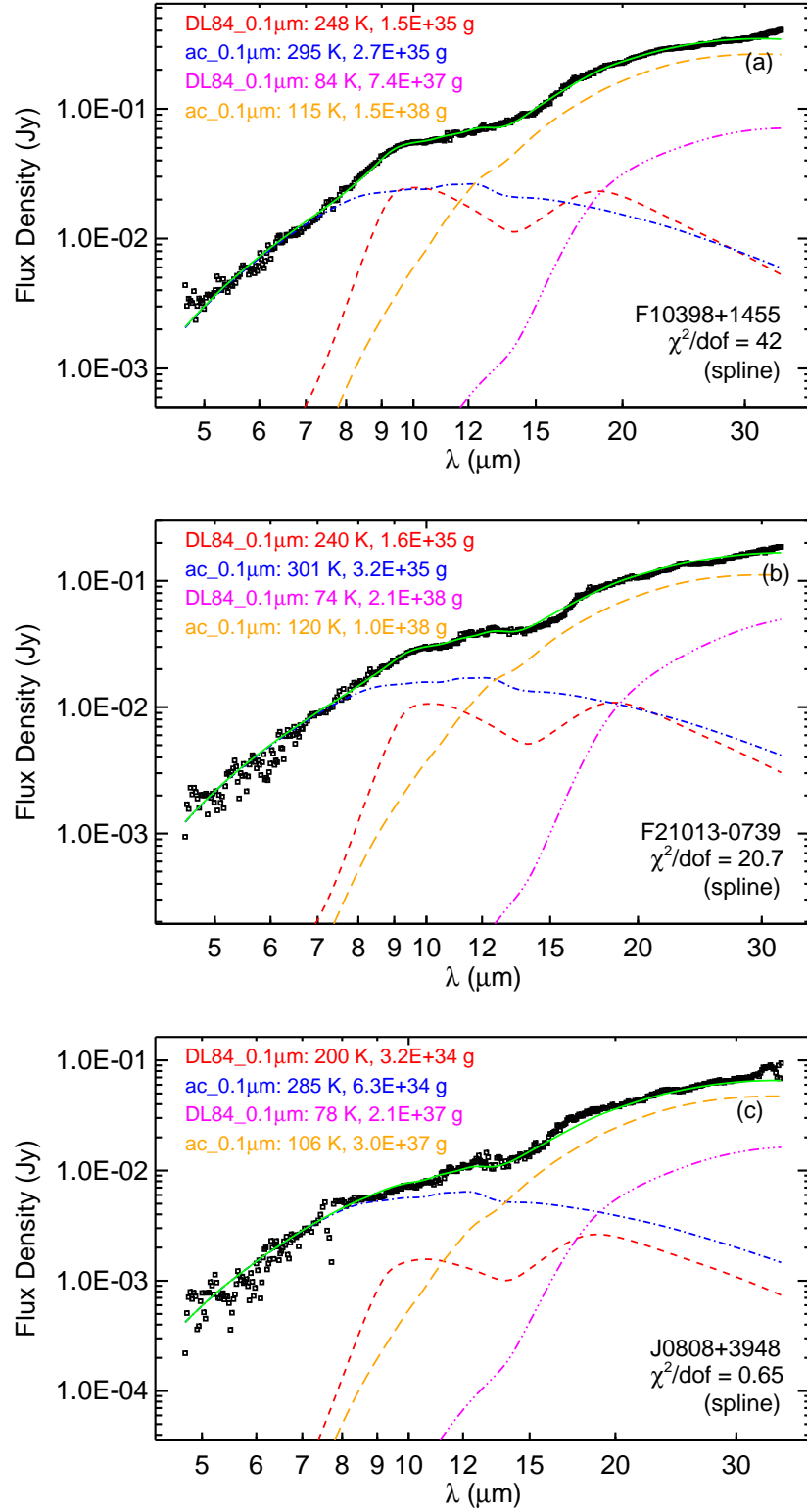


Fig. 12.— Same as Figure 4 but with the “observed” spectra (black open squares) obtained by subtracting from the *Spitzer*/IRS spectra the PAH and ionic emission lines determined with the spline method (see §1).

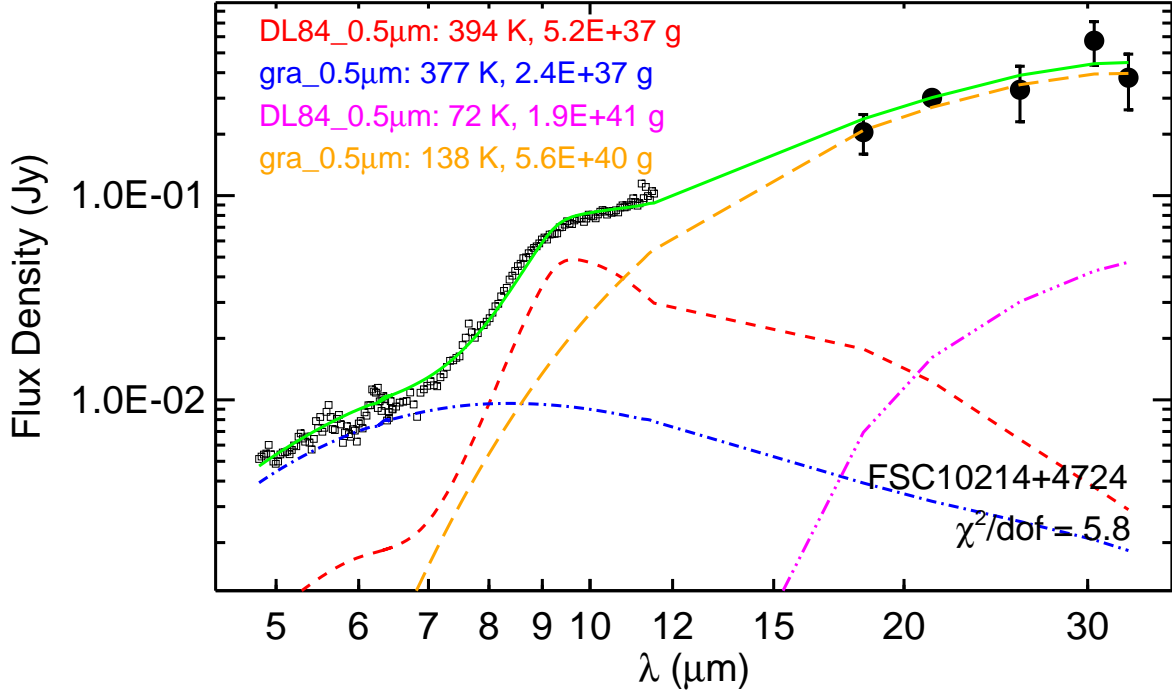


Fig. 13.— Comparison of the observed IR emission of IRAS FSC10214+4724 (black open squares; Teplitz et al. 2006) with the model emission (solid green line) which is a sum of four components: warm DL84 silicate (red dashed line), cold DL84 silicate (magenta dot-long dashed line), warm graphite (blue dotted-dashed line), and cold graphite (orange long dashed line). All dust components have a size of  $a = 0.5 \mu\text{m}$ .

## 5.2. Comparison with ULIRG and Quasars

The anomalous IR emission (i.e., a steep  $\sim 5\text{--}8 \mu\text{m}$  emission continuum combined with silicate emission) seen in IRAS F10398+1455, IRAS F21013-0739 and SDSS J0808+3948 is rarely seen in other sources. To the best of our knowledge, the only similar source is IRAS FSC 10214+4724, a lensed, starburst-powered ULIRG at a redshift of  $z \approx 2.29$  (Teplitz et al. 2006). The major difference between IRAS FSC 10214+4724 and our three galaxies is that IRAS FSC 10214+4724 lacks the PAH emission features which are prominent in our three galaxies. We have also modeled the IR emission of IRAS FSC 10214+4724. As shown in Figure 13, a mixture of warm/cold “astronomical silicate” and warm/cold graphite of  $a \approx 0.5 \mu\text{m}$  closely fits the observed IR emission. The derived parameters (see Table 2) are similar to that of our three galaxies.

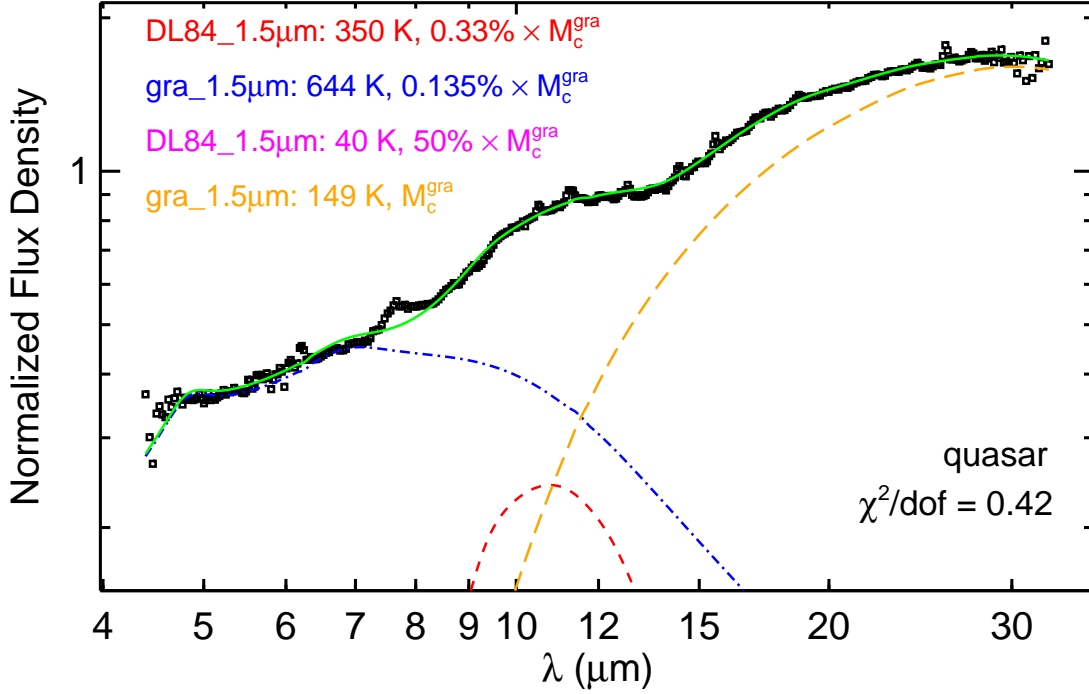


Fig. 14.— Same as Figure 13 but for the average spectrum of quasars (see Hao et al. 2007).

We have also modeled the average spectrum of quasars (Hao et al. 2007).<sup>7</sup> As shown in Figure 14, the average quasar spectrum exhibits a flat  $\sim 5\text{--}8\,\mu\text{m}$  emission continuum and a broad silicate emission feature at  $9.7\,\mu\text{m}$ . The best-fit is achieved with dust of  $a \approx 1.5\,\mu\text{m}$ , with  $T_w^S \approx 350\,\text{K}$  for warm silicate,  $T_w^C \approx 644\,\text{K}$  for warm graphite,  $T_c^S \approx 40\,\text{K}$  for cold silicate, and  $T_c^C \approx 149\,\text{K}$  for cold graphite. The flat  $\sim 5\text{--}8\,\mu\text{m}$  emission continuum seen in quasars is caused by warm graphite which is about twice as hot as that in our three galaxies.

In principal, it would be desirable to model the IR emission spectra of starbursts to which the steep  $\sim 5\text{--}8\,\mu\text{m}$  continuum emission and the PAH emission features of our three galaxies bear a close resemblance. However, to obtain any meaningful information about the properties of the dust (e.g., size, composition, temperature) from modeling the IR spectra of starbursts, one has to make assumptions concerning the distribution of stars and dust within the starburst. We therefore intend not to model the IR spectra of starbursts as we know little about how stars and dust are spatially distributed.

<sup>7</sup>The averaged spectrum of quasars is constructed with individual quasar spectra normalized at  $\lambda = 14.5\,\mu\text{m}$ , in order to avoid the most luminous quasar dominating the resulting spectrum.

Y. Xie et al. (2015, in preparation) examine the multi-wavelength data of these three galaxies to investigate their powering sources. They find that F21013-0739 and SDSS J0808+3948 have detections in hard X-rays (Jia et al. 2011) which indicates the presence of AGN. However, the diagnostics from the UV, optical, mid-IR, and radio do not show any strong evidence of AGN. They conclude that AGN may be present in these galaxies, but they are too young to be detected in all wavelength bands. The lower dust temperature ( $T \sim 250\text{--}400\text{ K}$ ) and smaller grain size (with an upper limit of  $a \lesssim 1.0\text{ }\mu\text{m}$ ) inferred for our three galaxies compared with that of quasars could be due to the fact that our galaxies may harbor a young/weak AGN which is not maturely developed yet. Compared with quasars, such a young AGN emits much less and softer in the X-ray and UV. Therefore, sub- $\mu\text{m}$ -sized grains could survive against sublimation and photo-sputtering in our galaxies while only  $\mu\text{m}$ -sized grains could survive in quasars. Exposed to a young AGN with a lower UV luminosity  $L_{\text{UV}}$ , the dust temperature is expected to be lower since  $T \propto L_{\text{UV}}^{1/(4+\beta)}$ , where  $\beta$  is the dust opacity power-law exponent in the far-IR (i.e.,  $\kappa_{\text{abs}} \propto \lambda^{-\beta}$ ). Indeed, the bolometric luminosity of our galaxies is in the order of  $\sim 10^{44}\text{ erg s}^{-1}$  (Y. Xie et al. 2015, in preparation), about two orders of magnitude lower than that of typical quasars.

## 6. Summary

We have modeled the *Spitzer*/IRS spectra of three spectroscopically anomalous galaxies (IRAS F10398+1455, IRAS F21013-0739 and SDSS J0808+3948) in terms of a simple model consisting of a mixture of warm and cold silicate dust, and warm and cold carbon dust. The IR spectral characteristics of these galaxies are unique in the sense that they show silicate emission which is characteristic of AGN while they also show a steep  $\sim 5\text{--}8\text{ }\mu\text{m}$  emission continuum and strong PAH emission features which are characteristic of starburst galaxies. In contrast, AGN exhibit a *flat* emission continuum at  $\sim 5\text{--}8\text{ }\mu\text{m}$  and lack the PAH emission features. The  $9.7$  and  $18\text{ }\mu\text{m}$  silicate features seen in emission in these three galaxies are seen in absorption in starbursts. We find that our model with four components (cold and warm carbons, cold and warm silicates) closely reproduces the observed IR emission of all three galaxies, including the steep  $\sim 5\text{--}8\text{ }\mu\text{m}$  emission continuum and the  $9.7\text{ }\mu\text{m}$  silicate emission feature. The model-fitting results are insensitive to the exact silicate and carbon dust composition (e.g., “astronomical” silicate or laboratory analogs, olivine or pyroxene, iron-poor silicate or iron-rich silicate, amorphous carbon or graphite) and dust size, provided the dust size does not exceed one micrometer (i.e.,  $a \lesssim 1.0\text{ }\mu\text{m}$ ). It is also found that the dust temperature is the primary cause in regulating the steep  $\sim 5\text{--}8\text{ }\mu\text{m}$  emission continuum and the prominent silicate emission feature. Compared with the average spectrum of quasars which exhibits a flat  $\sim 5\text{--}8\text{ }\mu\text{m}$  continuum, the steep  $\sim 5\text{--}8\text{ }\mu\text{m}$  continuum seen in our three

galaxies predominantly arises from warm carbon dust of temperatures of  $T \sim 250\text{--}400\text{ K}$ , much lower than that of quasars ( $T \sim 640\text{ K}$ ). The  $9.7\text{ }\mu\text{m}$  silicate emission of the quasar average spectrum is best fitted with silicate dust of size  $a \approx 1.5\text{ }\mu\text{m}$ , larger than the upper size limit of  $a \lesssim 1.0\text{ }\mu\text{m}$  inferred for our three galaxies. The lower dust temperature and smaller dust size inferred for our three galaxies compared with that of quasars could be due to the fact that our galaxies may harbor a young/weak AGN which is not maturely developed yet. To test the simple dust model used in current work, we would like to present a series of physical AGN models (e.g Clumpy models) for these three galaxies as well as the quasar average spectrum and ULIRG FSC 10214+4724 using the model parameters derived in this paper (R. Nikutta et al. 2015, in preparation).

We thank V. Charmandaris, A. Mishra, J. Y. Seok, S. Wang and the anonymous referee for helpful suggestions and discussions. L. H. and X. Y. X. are supported by the National Natural Science Foundation of China under grants No. 11473305, by the Strategic Priority Research Program "The Emergence of Cosmological Structures" of Chinese Academy of Sciences, Grant No. XDB09030200. A. L. and X. Y. X. are supported in part by NSF AST-1311804 and NASA NNX14AF68G. R. N. acknowledges support by FONDECYT grant No. 3140436. The Cornell Atlas of *Spitzer*/IRS Sources (CASSIS) is a product of the Infrared Science Center at Cornell University, supported by NASA and JPL.

## REFERENCES

- Allamandola, L. J., Tielens, A. G. G. M., & Barker, J. R. 1985, ApJ, 290, L25
- Antonucci, R. 1993, ARA&A, 31, 473
- Asplund, M., Grevesse, N., Sauval, A. J., & Scott, P. 2009, ARA&A, 47, 481
- Baldwin, J. A., Phillips, M. M., & Terlevich, R. 1981, PASP, 93, 5
- Bohren, C. F., & Huffman, D. R. 1983, Absorption and scattering of light by small particles
- Dorschner, J., Begemann, B., Henning, T., Jaeger, C., & Mutschke, H. 1995, A&A, 300, 503
- Draine, B. T., & Lee, H. M. 1984, ApJ, 285, 89
- Draine, B. T., & Li, A. 2001, ApJ, 551, 807
- Hao, L., Weedman, D. W., Spoon, H. W. W., et al. 2007, ApJ, 655, L77

- Henning, T. 2010, *ARA&A*, 48, 21
- Houck, J. R., Roellig, T. L., van Cleve, J., et al. 2004, *ApJS*, 154, 18
- Imanishi, M., Terada, H., Sugiyama, K., et al. 1997, *PASJ*, 49, 69
- Jia, J., Ptak, A., Heckman, T. M., et al. 2011, *ApJ*, 731, 55
- Köhler, M., & Li, A. 2010, *MNRAS*, 406, L6
- Laor, A., & Draine, B. T. 1993, *ApJ*, 402, 441
- Lebouteiller, V., Barry, D. J., Spoon, H. W. W., et al. 2011, *ApJS*, 196, 8
- Léger, A., & Puget, J. L. 1984, *A&A*, 137, L5
- Li, A. 2004a, in *Astrophysics of Dust* (ASP Conf. Ser. 309), ed. A.N. Witt, G.C. Clayton, & B.T. Draine (San Francisco, CA: ASP), 417
- Li, A. 2004b, in *Penetrating Bars Through Masks of Cosmic Dust: The Hubble Tuning Fork Strikes a New Note*, ed. D.L. Block, I. Puerari, K.C. Freeman, R. Groess, & E.K. Block (Dordrecht: Kluwer) 535
- Li, A. 2007, in *The Central Engine of Active Galactic Nuclei* (ASP Conf. Ser. 373), ed. L. C. Ho & J.-M. Wang (San Francisco, CA: ASP), 561
- Li, A. 2009, in *Small Bodies in Planetary Sciences* (Lecture Notes in Physics vol. 758), ed. I. Mann, A. Nakamura, & T. Mukai, Springer, Chapter 6, 167
- Li, M. P., Shi, Q. J., & Li, A. 2008, *MNRAS*, 391, L49
- Lyu, J., Hao, L., & Li, A. 2014, *ApJ*, 792, L9
- Maiolino, R., Marconi, A., & Oliva, E. 2001, *A&A*, 365, 37
- Markwardt, C. B. 2009, in *Astronomical Data Analysis Software and Systems XVIII* (ASP Conf. Ser. 411), ed. D. A. Bohlender, D. Durand, & P. Dowler (San Francisco, CA: ASP), 251
- Markwick-Kemper, F., Gallagher, S. C., Hines, D. C., & Bouwman, J. 2007, *ApJ*, 668, L107
- Mason, R. E., Wright, G., Pendleton, Y., & Adamson, A. 2004, *ApJ*, 613, 770
- Mason, R. E., Levenson, N. A., Shi, Y., et al. 2009, *ApJ*, 693, L136

- Mason, R. E., Rodriguez-Ardila, A., Martins, L., et al. 2015, *ApJS*, 217, 13
- Nikutta, R., Elitzur, M., & Lacy, M. 2009, *ApJ*, 707, 1550
- Pendleton, Y. J., & Allamandola, L. J. 2002, *ApJS*, 138, 75
- Roche, P. F., Aitken, D. K., Smith, C. H., & Ward, M. J. 1991, *MNRAS*, 606, 629
- Rouleau, F., & Martin, P. G. 1991, *ApJ*, 377 526
- Siebenmorgen, R., Krügel, E., & Spoon H. W. W. 2004, *A&A*, 414, 123
- Smith, J. D. T., Draine, B. T., Dale, D. A., et al. 2007, *ApJ*, 656, 770
- Smith, H. A., Li, A., Li, M. P., et al. 2010, *ApJ*, 716, 490
- Sofia, U. J., Parvathi, V. S., Babu, B. R. S., & Murthy, J. 2011, *AJ*, 141, 22
- Spoon, H. W. W., Armus, L., Cami, J., et al. 2004, *ApJS*, 154, 184
- Sturm, E., Hasinger, G., Lehmann, I., et al. 2006, *ApJ*, 642, 81
- Teplitz, H. I., Armus, L., Soifer, B. T., et al. 2006, *ApJ*, 638, L1
- Urry, C. M., & Padovani, P. 1995, *PASP*, 107, 803
- Voit, G. M. 1991, *ApJ*, 379, 122
- Voit, G. M. 1992, *MNRAS*, 258, 841
- Xie, Y., Hao, L., & Li, A. 2014, *ApJ*, 794, L19